
Doctoral Dissertations

Student Theses and Dissertations

Fall 2014

Radio frequency interference (RFI) modeling of complex modules in mobile devices and system-level modeling for transient ESD simulation

Tianqi Li

Follow this and additional works at: https://scholarsmine.mst.edu/doctoral_dissertations



Part of the [Electrical and Computer Engineering Commons](#)

Department: **Electrical and Computer Engineering**

Recommended Citation

Li, Tianqi, "Radio frequency interference (RFI) modeling of complex modules in mobile devices and system-level modeling for transient ESD simulation" (2014). *Doctoral Dissertations*. 2346.
https://scholarsmine.mst.edu/doctoral_dissertations/2346

This thesis is brought to you by Scholars' Mine, a service of the Missouri S&T Library and Learning Resources. This work is protected by U. S. Copyright Law. Unauthorized use including reproduction for redistribution requires the permission of the copyright holder. For more information, please contact scholarsmine@mst.edu.

RADIO FREQUENCY INTERFERENCE (RFI) MODELING OF COMPLEX
MODULES IN MOBILE DEVICES
AND SYSTEM-LEVEL MODELING FOR TRANSIENT ESD SIMULATION

by

TIANQI LI

A DISSERTATION

Presented to the Faculty of the Graduate School of the
MISSOURI UNIVERSITY OF SCIENCE AND TECHNOLOGY

In Partial Fulfillment of the Requirements for the Degree

DOCTOR OF PHILOSOPHY

in

ELECTRICAL ENGINEERING

2014

Approved by

Dr. David J. Pommerenke, Advisor

Dr. Victor Khilkevich

Dr. Jun Fan

Dr. Daryl Beetner

Dr. Stephan Frei

© 2014

Tianqi Li

All Rights Reserved

PUBLICATION DISSERTATION OPTION

This dissertation consists of the following three papers, formatted in the style used by the Missouri University of Science and Technology, listed as follows:

Paper 1, T. Li, V. Khilkevich, “Phase-resolved Near Field Scan over Random Fields”, submitted to IEEE Trans. on EMC., 2014.

Paper 2, T. Li, A. Patnaik, S. Marathe, G. Maghlakelidze, V. Khilkevich, D. J. Pommerenke, “Radio Frequency Interference Modeling of Complex Modules in Mobile Devices”, submitted to IEEE Trans. on EMC., 2014.

Paper 3, T. Li, V. Pilla, Z. Li., D. J. Pommerenke, S. Hideki, J. Maeshima, K. Araki, “System-Level Modeling for Transient Electrostatic-Discharge (ESD)Simulation”, submitted to IEEE Trans. on EMC., 2014.

ABSTRACT

The thesis is composed of three papers, which cover the systematic modeling of radio-frequency-interference (RFI) and electro-static-discharge (ESD) problems happened in mobile devices.

In the first paper, an averaging technique is developed, for phase resolved scanning over random fields generated by multiple uncorrelated stochastic sources. This method can separate the field contribution of each noise source and resulting field patterns as if the out-of-interest sources were turned off. The scanned data can be used for emission source localization, far-field pattern calculation and Huygens's box modeling.

In the second paper, using Huygens's Equivalent Theorem a systematic approach for the modeling of radio frequency interference is introduced. The methodology can be implemented using commercial tools and thereby does not require any additional data handling algorithm, e.g. extracting dipole moments from the scanned data. The influence of multiple-scattering effects is considered. The challenges of modeling a complex electronic system are summarized and solutions are provided.

In the third paper, an improved electrostatic discharge (ESD) system-level transient simulation modeling method and discusses its validation using IEC 61000-4-2 ESD pulses on a real-world product. The system model is composed of high current and broadband (up to 3GHz) models of R, L, C, ferrite beads, diodes, and integrated circuit IO pins. A complex return path model is the key to correctly modeling the system's response to the IEC excitation. The model includes energy-limited, time-dependent IC damage models. A power-time integral method is introduced to accurately determine if a junction would experience thermal runaway under an arbitrary injection waveform.

ACKNOWLEDGMENTS

I would like to express my sincere gratitude to Dr. David J. Pommerenke, my advisor, for his guidance and instruction on my research work, financial support to my study and direction for this thesis during my pursuit of the PhD's degree.

I would like to thank Dr. Victor Khilkevich, for the substantial help and guidance on my research.

I would like to thank Dr. Jun Fan, Dr. Daryl Beetner and Dr. James Drewniak, for their teaching in my courses, discussions related to my research and helpful suggestions on my thesis.

I would like to thank Dr. Stephan Frei, my committee member, for the discussion and helpful suggestions on my research.

I would also like to express my thanks to all the other faculty members and students in the UMR/MST EMC lab for their team work and help in my research and coursework.

Finally, I would like to thank my family for their endless love and support in my whole life. I would thank my fiancée Xinyun Guo for her unconditional support and love during my PhD study.

TABLE OF CONTENTS

	Page
PUBLICATION DISSERTATION OPTION.....	iii
ABSTRACT.....	iv
ACKNOWLEDGMENTS.....	v
LIST OF ILLUSTRATIONS.....	x
SECTION	
1. INTRODUCTION.....	1
PAPER	
I. Phase-Resolved Near Field Scan Over Random Fields.....	4
Abstract.....	4
I. INTRODUCTION.....	4
II. METHODOLOGY.....	5
III. EXPERIMENTAL VALIDATION.....	9
IV. APPLICATIONS OF THE AVERAGING NFS METHOD.....	13
A. Emission Source Microscopy.....	13
B. Near Field to Far Field Transformation.....	13
V. CONCLUSION.....	14
REFERENCES.....	16
II. Radio Frequency Interference Modeling of Complex Modules in Mobile Devices....	19
Abstract.....	19
I. INTRODUCTION.....	20
II. THE MODELING METHODOLOGY.....	23

A. The Generalized RFI Modeling Workflow.....	23
B. A Metal Structure Passes Through a Huygens's Boundary.....	27
C. Testing the Tangential Fields over a Huygens's Surface.....	28
III. METHODOLOGY VALIDATION.....	30
A. Numerical Validation.....	30
B. Experimental Validation.....	31
IV. MODELING AN ACTIVE LCD IN A REAL CELLPHONE CONTEXT....	36
A. Introduction to the Cellphone Under Investigation.....	36
B. Structure of the LCD.....	38
C. Modelling the Active LCD with a Huygens's Box.....	39
V. DISCUSSION.....	42
VI. CONCLUSION.....	44
REFERENCES.....	44
III. System-Level Modeling for Transient Electrostatic-Discharge Simulation.....	48
Abstract.....	48
I. INTRODUCTION.....	49
II. SYSTEM UNDER INVESTIGATION.....	51
III. MODELING METHODOLOGY.....	52
IV. COMPONENT MODELS.....	54
A. Semiconductor Devices.....	54
B. Capacitors, Ferrite Beads and Inductors.....	57
V. DYNAMIC DESTRUCTION THRESHOLD MODELING.....	62
A. Failure Power Models.....	62
B. Failure Criteria.....	65

VI. SYSTEM LEVEL SETUP, ESD GUN MODEL AND COMMON MODE MODELING.....	68
A. System-Level Test Setup and Modeling.....	68
B. System-Level Grounding Model.....	68
C. ESD Gun Model.....	69
VII. SYSTEM LEVEL SIMULATION RESULTS.....	71
A. System Model Validation.....	71
B. Application of the System Model for ESD Hard-Error Analysis.....	73
VIII. CONCLUSION.....	75
REFERENCES.....	76
SECTION	
2. CONCLUSION.....	80
VITA.....	82

LIST OF ILLUSTRATIONS

Figure	Page
PAPER I	
1. Numerical results of (6) with different denominator SNRs.	8
2. Proposed two-probe-setup for phase-resolved NFS over multiple uncorrelated noise sources.	9
3. Phase-resolved scanning test setup over two uncorrelated noises.	10
4. Layout of the PCB under test. Ports 1 and 2 are the excitation ports of the U-shaped trace and the patch, respectively.	11
5. Power spectra of the random signals injected into (top) the trace and (mid) the patch.	11
6. (a) The scanning probe's output when both the trace and the patch were excited concurrently with uncorrelated random signals; (b) the proposed method by taking $\langle v_1/v_2 \rangle$, as the reference probe placed near the patch; (c) the scanned data when the patch was excited solely; and (d) the simulation result of the patch's near field.	15
7. Calculated focus fields (mV/m) at the source plane ($z=0\text{mm}$) with the scanned data acquired when the reference probe was placed near the patch.	16
8. The patch's far-field pattern.	16
PAPER II	
1. An LCD's internal structure.	21
2. An arbitrary source and a victim placed in space.	24
3. Setup for solving radiation fields (\vec{E}_1, \vec{H}_1).	25
4. Models for solving the coupled noise into the victim: (a) without and (b) with the multiple-scattering effect.	26
5. The proposed RFI modeling work flow.	28

6. Side view of two microstrips referencing the same ground plate that has a limited size.	28
7. The geometry created for numerically validating the proposed method.	32
8. The coupling result of Huygens's equivalent model compared to the direct model.	32
9. Block diagram and layout of the phase-resolved scan over a 120mm×51mm patch.	33
10. Calculated real part of the E-field at 13.5 mm above the bottom plate at a given phase: (top row) direct model vs. (bottom row) the Huygens's box model.	33
11. Calculated RFI coupling to surrounding imaginary dipoles and monopoles.	34
12. Test setup for modeling a real LCD under passive mode.	35
13. The victim antenna's return loss, measured vs. simulated.	35
14. RFI result of the setup shown in Fig. 12, measured vs. calculated with the proposed Huygens's box model.	36
15. (top) Test setup to check a phone's RFI, and (bottom) the tested RFI caused by the LCD operation; max hold was used, and RBW=2KHz. The data was uncalibrated.	37
16. Simplified cell phone structure: (left) backside view, without the back cover and battery, and (right) LCD-side view.	38
17. (left) Bottom view and (mid) top view of the setup built for characterizing the LCD, and (right) full-wave model of this setup (the copper plate is hidden from view).	40
18. Z_{11} of the Fig. 17 setup, when the LCD panel's $\sigma = 1000s/m$	40
19. Phase-resolving scanning setup for testing the active LCD.	41
20. Scanned tangential fields (H_x , H_y) at 903.76MHz at 3mm above the active LCD.	42
21 (top) the complete cellphone RFI model and (bottom) its internal details.	43

1. The layout of the cell phone's keyboard backlight circuit.	52
2. Complete modeling framework for every device.	53
3. One of the automatic TLP systems used to capture the voltage and current pulse of a DUT.	53
4. (top) Model of the Zener diode, and (bottom) transient I-V characteristics of the Zener diode, simulated vs. measured.	55
5. (top) LED model and (bottom) its I/V curve.	56
6. (a) IO pin model and (b) transient I-V characteristics of the IO pin, simulated vs. measured.	57
7. Voltage and current of a 10V-rated X7R 10nF capacitor excited by a 15ns wide TLP pulse at 3kV charge voltage.	58
8. Capacitance-voltage nonlinear relation, $C(V)$, of the 10V-rated 10nF X7R capacitor, simulated vs. measured.	59
9. Inductance as a function of current defined using Eq. (4).	61
10. Nonlinear model of a ferrite bead.	62
11. Tested time-dependent damage threshold of the driver IC in terms of its through current.	63
12. Junction damage power versus rectangular pulse width [23].	64
13. Time-dependent damage threshold of the InGaN white LED in terms of its injection power, measured vs. modeled.	64
14. Time-dependent damage threshold of the LED driver's IO pin in terms of its injection power, measured vs. modeled.	65
15. The schematic of contact-mode discharge setup on the cellphone LED.	69
16. System-level modeling structure.	69
17. Equivalent circuit model of the ESD generator.	70
18. Schematic of system-model validation setup.	71
19. IO pin's current under ESD injection at the cathode of the LED, simulated vs. measured.	73

20. Simulated injection power into LED under ESD contact-mode discharge at the LED's cathode.	74
21. Determine LED's damage with (13), which yielded the same conclusion with Fig. 20.	74
22. Simulated injection power into LED driver's IO pin without any external protection under ESD contact-mode discharge at the LED's cathode (same setup as in Fig. 18).	75

1. INTRODUCTION

Intra-system electromagnetic compatibility (EMC) or Radio-Frequency Interference (RFI) is one of the challenging problems in modern electronics. For example, a mobile phone antenna and its receiver form an RF module, that can detect signals as weak as -120dBm in a 200KHz bandwidth, if not disturbed by nearby electronics. However, the clock frequencies of a smart phone can reach GSM880, or even GSM1800. The harmonics and data signals couple to the antenna and de-sensitize (de-sense) the RF system and thereby degrading the communication quality.

RFI modeling is necessary for optimizing the victim antenna design, location, grounding/shielding structures, and system floor planning at the early design phase. A noisy integrated circuit (IC) can be modeled directly if there's sufficient IC information. However, in many practical cases, the noise source's internal information may be unknown, or even if it is known, the source maybe too complex to model. Besides structural complexity, the module is behaviorally complex. An active circuit may show different RFI signatures when it is displaying different photos and these signatures may appear as a time varying and stochastic fashion.

In this dissertation, a systematic approach is proposed to model the RFI. This solution path combines the Huygens principle with correction for multiple-scattering, sensitive resonant probes, reconstruction of E-field from H-field only scan and the handling of random-like signals to form a novel method that allows to model the RFI coupling within a complex system. We start by examining the rational and then validate the method based using numerical and experimental examples. To demonstrate the application of the proposed method, the coupling from an active LCD to the antenna

within a cell phone is simulated and compared to measurements.

Electro-static discharge (ESD) is another challenging problem in mobile devices. Recent studies have shown that system-level electrostatic discharge (ESD) simulation can serve as a powerful tool for analyzing ESD performance. The simulation enables the design of reliable protection on the first attempt and avoids the need for repeated design optimization tests.

The concept of ESD simulation has been promoted as an option in system-level ESD efficient design (SEED). Although the SEED simulation offers greatly improved system-level ESD design, some issues remain unresolved. Firstly, TLP-derived IC data show good repeatability due to the simplicity of the TLP waveform. However, the waveform does not resemble real ESD waveforms. To further optimize the design methodology, one should perform the characterization and simulation using the waveform described in IEC 61000-4-2, or Human Machine Model (HMM) excitation for setting up the ESD simulation.

It is difficult to convert a TLP-based simulation into an IEC setup directly by substituting the TLP model with an ESD gun model. Compared to a TLP-based model, an IEC source-based setup requires more sophisticated modeling on the current return path in order to achieve an accurate circuit response under ESD tests. Furthermore, intensive use of flex-printed-circuits (FPCs) for connecting multiple PCBs creates complex return paths.

This dissertation consists of three papers which focus on the above two topics. Paper 1 proposes a new near field scanning technique for phase resolved scan over multiple uncorrelated noise sources. This technique lays the cornerstone for modeling a

complex noise source with its emitted near field. Paper 2 proposes a systematic approach to model a complex noise source, an LCD, for calculating the RFI to nearby antenna inside a phone system. Paper 3 proposes a systematic method to model the ESD current flow through inside a complex system under IEC-61000-4-2 excitation. It also introduces a thermal model to determine the device hard error due to the ESD event.

The primary contributions of this dissertation include:

A new method for scanning over multiple random noise sources (paper 1).

A systematic approach is proposed to model a complex noise source with Huygens's equivalent theorem (paper 2).

A method is developed accounting for multiple scattering effects between the source and the victim (paper 2).

A systematic methodology is developed to model R, L, C, Ferrite devices for ESD simulation (paper 3).

A system return path modeling method for ESD calculation (paper 3).

A method, developed from applying the Green's Function, for determine if a device would experience thermal runaway from ESD injection. (paper 3).

PAPER

I. Phase-resolved Near Field Scan over Random Fields

Tianqi Li, *Student Member, IEEE*, Victor Khilkevich, *Member, IEEE*

Abstract— This paper discusses an averaging technique for phase-resolved scanning of fields generated by multiple, uncorrelated stochastic sources. This method can separate the field contribution of each noise source into the resulting field patterns as if the sources that are not of interest were turned off. The scanned data can be used to localize the emission source and to calculate the far-field pattern and total power.

Index Terms— Electromagnetic Compatibility, Near-Field Scan, Far Field, Emission Source Microscopy, Random Fields

I. INTRODUCTION

Phase-resolved near-field scanning (NFS) has been used widely in electromagnetics and antenna research. Yaghjian thoroughly reviewed near-field antenna measurements for antenna pattern analysis [1]. Several researchers have proposed methods by which to extract dipole moments from the scanned near field in order to perform far-field calculations [2]. The scanned data also can be used to identify emission sources, e.g., Emission Source Microscopy (ESM) [3], or to build a Huygens's box model as an equivalent to the actual source [4].

The existing NFS-related studies were performed mainly on well-defined sources. Challenges may arise when conducting NFS on real-world products, which could contain a number of active circuits that generate random, time-variant and modulated fields. These noises could emit within the same frequency band and contribute to far-field

emission concurrently. Direct scanning over such a product may lead to incorrect results. Research investigating NFS of stochastic fields is rare. Arnaut and Obiekezie have developed a stochastic method for source identification and pair-wise space-frequency correlation between dipole sources [5].

In this paper, we propose a simple yet effective method, based on averaging over realizations, to separate multiple, uncorrelated noise sources during phase-resolved NFS. As a result, the tested field pattern can be acquired as if out-of-interest sources were turned off.

II. METHODOLOGY

Consider two sources of electromagnetic fields driven by uncorrelated random signals x_1 and x_2 , and then suppose that two measurements are performed, one with a scanning probe and one with a reference probe. The probe outputs are linear combinations of the source signals: $v_1 = k_{11}x_1 + k_{12}x_2$ for the scanning probe, and $v_2 = k_{21}x_1 + k_{22}x_2$ for the reference probe. The coefficients k_{ij} depend on the positions of the probes and whether or not the scanning probe is moved over a certain surface; the coefficient k_{11} will reflect the amplitude and phase variations of the electromagnetic field on that surface. The goal of the scanning is to determine the coefficients k_{11} and k_{12} .

The ratio of the probe outputs is given by

$$\frac{v_1}{v_2} = \frac{k_{11}x_1 + k_{12}x_2}{k_{21}x_1 + k_{22}x_2} \quad (1)$$

Consider a special case in which the reference probe is coupled to only one source, for example, x_1 , so $k_{22}=0$. In this case, (1) results in

$$\frac{v_1}{v_2} = \frac{k_{11}x_1 + k_{12}x_2}{k_{21}x_1} = \frac{k_{11}}{k_{21}} + \frac{k_{12}x_2}{k_{21}x_1} \quad (2)$$

If x_1 and x_2 are random variables with normal distributions and a zero mean, the ratio x_2/x_1 will be a random variable with Cauchy distribution with the probability density function

$$f(x) = \frac{1}{\pi} \left[\frac{\gamma}{(x-x_0)^2 + \gamma^2} \right] \quad (3)$$

where $x_0=0$ is the parameter that determines the location of the peak of the distribution, and γ is the parameter that specifies the width of the distribution. The mean value of the variable with Cauchy distribution does not exist because the integral

$$\langle x \rangle = \int_{-\infty}^{\infty} x f(x) dx = \frac{1}{\pi} \int_{-\infty}^{\infty} \frac{\gamma x}{(x-x_0)^2 + \gamma^2} dx \quad (4)$$

does not converge absolutely. However, if the values of the variables x_1 and x_2 are obtained in the measurement, only finite ratios of x_1 to x_2 can be registered. Therefore, the integration in (4) can be performed over the limited interval, and the expected value can be obtained as follows:

$$\langle x \rangle = \frac{1}{\pi} \int_{-B}^B \frac{\gamma x}{(x-x_0)^2 + \gamma^2} dx \quad (5)$$

where B is the largest possible value of the ratio of x_1 to x_2 , determined by the dynamic range of the measurement instrument. If $x_0=0$ (which is the case when x_1 and x_2 have zero means), the expected value of the ratio x_2/x_1 is zero because the integrand in (5) is an odd function and the integration limits are symmetrical. Therefore, the arithmetic mean of the measured samples of the ratio v_1/v_2 will converge to k_{11}/k_{21} :

$$\langle \frac{v_1}{v_2} \rangle = \lim_{N \rightarrow \infty} \frac{1}{N} \sum_{i=1}^N \frac{v_1^i}{v_2^i} = \frac{k_{11}}{k_{21}} \quad (6)$$

where v^i are samples of voltages, and N is the number of measurements.

According to (6), the averaged ratio of the scanning to the reference probe outputs yields a number that is proportional to the complex magnitude of the EM-field distribution on the scanning surface, at a single frequency.

Equation (6) was derived under the assumption that $k_{22}=0$, which is unachievable in practical experiments. In practice, the reference probe is always coupled to both signals. However, if the coefficient k_{22} is small enough (i.e., the signal-to-noise ratio (SNR) in the reference channel is high), then the estimation according to (6) will be practically accurate. To demonstrate this, a number of numerical experiments with different SNRs in the reference channels were conducted. In Matlab [6], the reference channel signal was constructed with

$$v_2 = k_{21}x_1 + n_2 = k_{21}(x'_1 + jx''_1) + M(n'_2 + jn''_2) \quad (7)$$

where x_1 is the signal and n_2 is the noise; x'_1, x''_1, n'_2, n''_2 are real-valued independent random sequences with a length of N and the same distribution; M is a real-valued constant coefficient to amplify the noise. Thus, the SNR of the reference signal v_2 was defined as $|k_{21}|/M$. The signal in the scanning probe was composed in the same way, while its SNR was selected as 1 (for simplicity). Because the transfer coefficients of the probes were selected as $k_{11}=1 \angle 17^\circ$ and $k_{21}=1 \angle -86^\circ$, the $\langle v_1/v_2 \rangle = k_{11}/k_{22} = 1 \angle 103^\circ$. Fig. 1 confirms that when the reference channel SNR is sufficiently large, the average ratio of voltages converges to the ratio k_{11}/k_{21} .

The above analysis can be migrated to multiple noise sources co-existing on a PCB, as shown in Fig. 2, in which source 1 was assumed to be of interest. The averaged v_1/v_2 converges to k_{11}/k_{21} when the coupling of reference probe 2 to other unwanted noises is negligible.

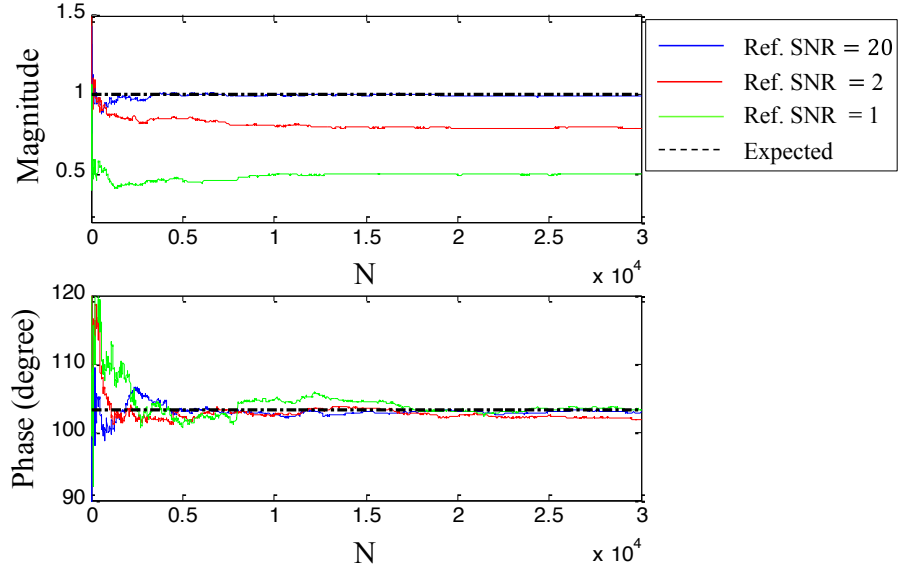


Fig. 1. Numerical results of (6) with different reference channel SNRs.

After acquiring the converged k_{11}/k_{21} , the phase of the scanned field can be obtained directly by taking angle (k_{11}/k_{21}). The field's absolute magnitude must be calibrated with the probing factor, P , of the scanning probe. The magnitude calibration can be derived as

$$\langle |E_1| \rangle = \langle |v_1| \rangle * P = \langle |k_{11}x_1| \rangle * P \quad (8)$$

where E_1 is the field excited by source x_1 . The source can be expressed with the reference probe's output as $x_1 = v_2/k_{21}$, so substituting x_1 into (8) yields

$$\langle |E_1| \rangle = \langle \left| \frac{k_{11}v_2}{k_{21}} \right| \rangle * P = \langle |v_2| \rangle * \left| \frac{k_{11}}{k_{21}} \right| * P \quad (9)$$

Then, the averaged field magnitude $\langle |E_1| \rangle$ can be calculated. This process does not require knowledge of the probe factor of the reference probe. The reference probe can be arbitrary, as long as it does not sense the unwanted sources.

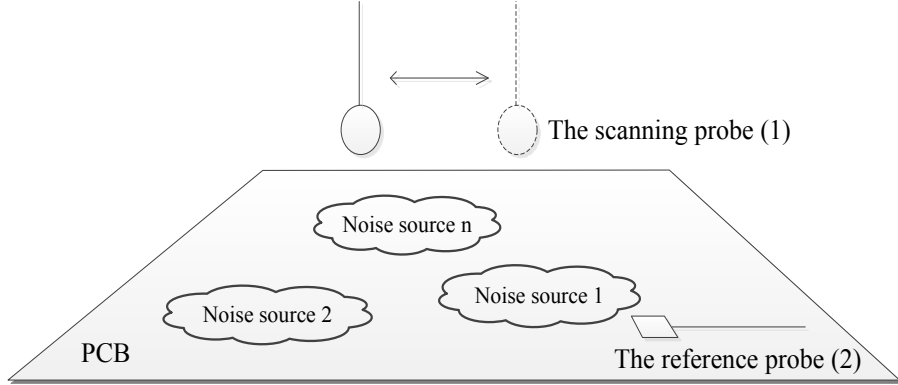


Fig. 2. Two-probe setup for phase-resolved NFS over multiple, uncorrelated noise sources.

III. EXPERIMENTAL VALIDATION

A setup (Fig. 3) was built to validate the NFS method. The printed circuit board (PCB) (Fig. 4) included two source structures, a U-shaped trace and a rectangular patch. The two structures were excited with two random signals, respectively. These signals were generated by modulating 3GHz carriers with normally distributed random signals (Fig. 5).

Because two random signals were generated by the same unit (two channels of the arbitrary waveform generator), it needed to be ensured that the signals were indeed not correlated. To achieve this verification, the coherence function between the two signals was measured. The measurement showed the value of the coherence function of -40 dB within the frequency range of interest, which was considered sufficiently low to represent uncorrelated signals (as the coherence function can take values between 1 for fully correlated signals and 0 for uncorrelated signals).

Both the trace and the patch noise fields were collected by the scanning probe, a 2~10 GHz log periodic dipole array (LPDA) antenna. The antenna factor (AF) of this

probe equaled 33dB m^{-1} . The reference probe, a 5×5 mm square loop, was placed very close to the patch and later to the trace. The LPDA's output was partially correlated with the reference probe's output. The uncorrelated portion, or the field attributed to the trace, was eliminated by taking the average of A/B, as described in Sec. II. In this way, the E_x and E_y patterns caused by the patch were obtained.

The vector network analyzer (VNA), Agilent N5245A, was set to tuned receiver mode to capture both probes' outputs. In this mode, the VNA acted like a vectorized dual-channel spectrum analyzer. The VNA's center frequency was set to 3GHz with zero-span, and 3201 sweeping points were used. In this way, this setup was equivalent to taking 3201 consecutive measurements at 3GHz. The VNA was synchronized with the two carrier generators to avoid frequency drift among them.

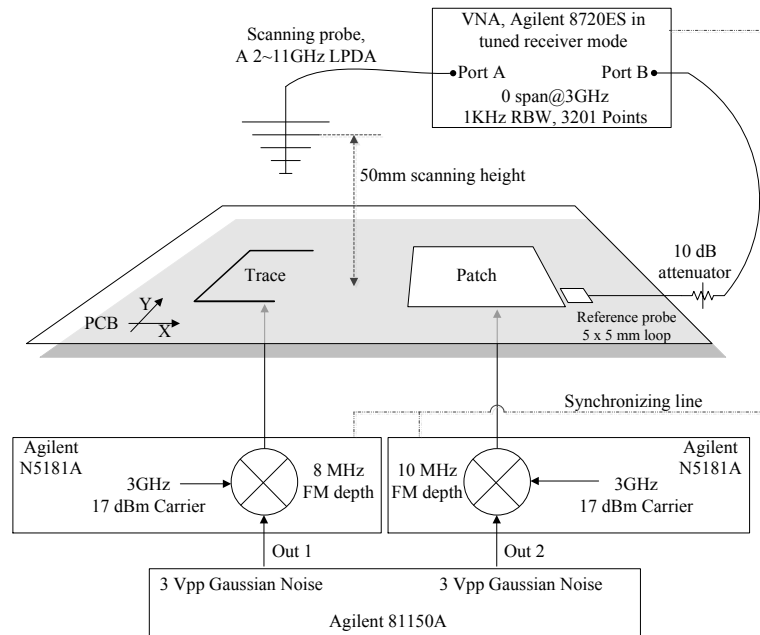


Fig. 3. Phase-resolved scanning test setup over two uncorrelated noises. The reference probe was placed close to either the patch or the trace, depending on which signal was of interest.

Fewer sweeping points could be used to reduce the overall scanning time, as long as the resulting SNR is acceptable. The settings of the sweeping points and resolution bandwidth (RBW) should be application specific, requiring *a priori* knowledge to scan a specific product.

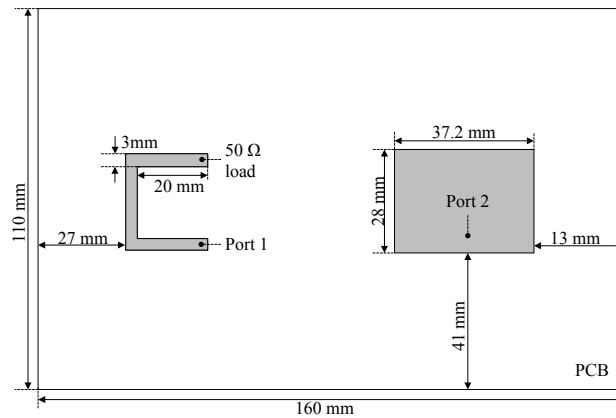


Fig. 4. Layout of the PCB under test. Ports 1 and 2 are the excitation ports of the U-shaped trace and the patch, respectively. The SMA connectors of the ports are located at the back side of this PCB.

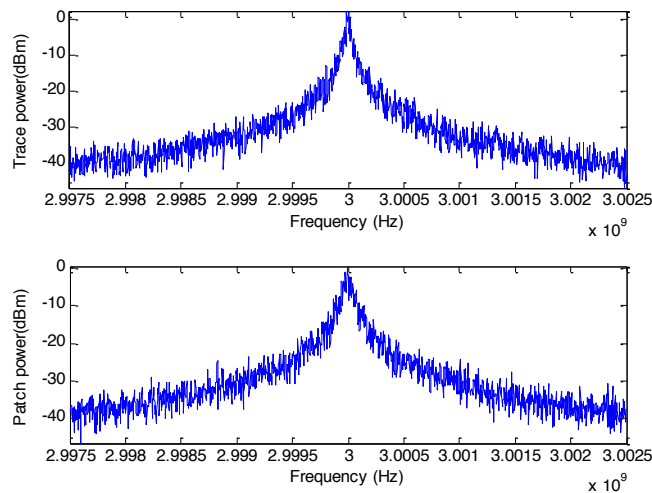


Fig. 5. Power spectra of the random signals injected into (top) the trace and (mid) the patch. The two signals were considered uncorrelated as their coherence function was less than -40 dB.

Two steps could be easily neglected, leading to incorrect or less valuable results. Firstly, ports A and B must be triggered at the same time; otherwise, the transfer function between them cannot be calculated due to the time-variant nature of the noise source. Secondly, the attenuator in front of port B (reference channel) should be selected deliberately such that similar power levels exist at both ports at the field's dominant region. The VNA can thereby operate within its maximal phase accuracy range [7].

The planar scanning height and extent were set according to Wang's study [8], which discussed the NFS inaccuracies attributed to different scanning heights, extents and steps. In this study, the scanning height was set at 0.5λ (50mm), and the scanning area was approximately $4\lambda \times 4\lambda$ (400mm \times 400mm). The scanning spatial step was set to 0.1λ (10mm).

As expected, the scanned raw data (Fig. 6a) showed very noisy patterns above both the trace and the patch. However, the data processed by averaging the A/B method (Fig. 6b) showed patterns very similar to those of the scanned result when the patch was excited solely (Fig. 6c). The results of the proposed method also agreed with those of the simulation (Fig. 6d).

Observable noises existed on the processed result on Ex. However, as will be illustrated later, these noises introduced limited error on the ESM and far-field calculation.

Using the same method, the trace contribution to the near field can also be measured by placing the reference probe close to the trace. The results of this measurement are not shown here for the sake of brevity.

IV. APPLICATIONS OF THE AVERAGING NFS METHOD

A. Emission Source Microscopy

The scanned field pattern can be used to identify the locations of radiative sources using the ESM algorithm [3]:

$$E(x, y, 0) = F^{-1}[F\{E(x, y, z)\} \times e^{jk_z z}] \quad (10)$$

where F stands for the spatial 2D Fourier transformation. This equation describes an inversely propagating wave with the $e^{jk_z z}$ term. The resulting $E(x, y, 0)$ is called the focus field because it focuses on the source position.

The focus fields calculated at the $z=0$ mm source plane (Fig. 7) using the processed NFS data correctly showed the expected emitting source. When the reference probe was placed close to the patch, the processed NFS data was the patch emission; therefore, the calculated focus field was on the patch.

B. Near-Field to Far-Field Transformation

The scanned near-field pattern can also be used for near-field to far-field transformation, and many techniques exist for this purpose [9][10][11]. Here, the Surface Equivalence Theorem [2] was used with the aid of CST's microwave studio [12]. By imprinting the scanned tangential E-field onto a perfect-electric-conductor (PEC) boundary, the far-field was calculated directly without the need for H-field measurements. Fig. 8 shows the near-field to far-field transformation result with the test data, versus the simulation results. The measurement agreed with the simulation reasonably well.

V. CONCLUSION

Averaging has been demonstrated as a convenient method for phase-resolved scanning when multiple random sources exist. This technique is useful in real-world applications because a product usually includes multiple active circuits with different emission signatures. The noise sources can be separated by selecting a reference probe site deliberately during the scan. Important VNA settings for such a test have been discussed. The far-field pattern caused by each source can be calculated accordingly from the scanned near-field data. Moreover, the scanned data in the semi-far-field region also allows the emission sources to be located using the ESM algorithm.

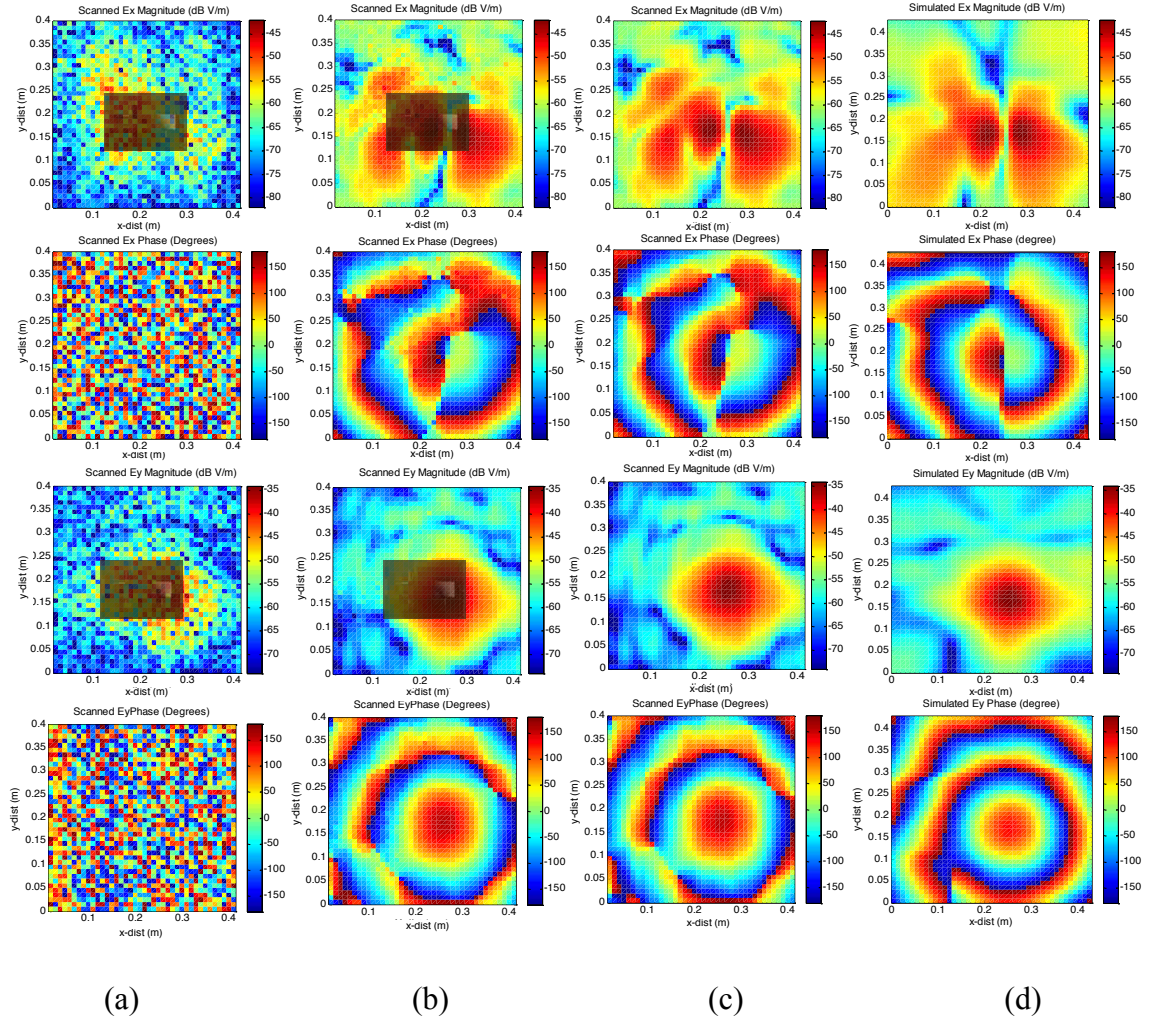


Fig. 6. (a) The scanning probe's output when both the trace and the patch were excited concurrently with uncorrelated random signals; (b) the proposed method by taking $\langle v_1/v_2 \rangle$, as the reference probe placed near the patch; (c) the scanned data when the patch was excited solely; and (d) the simulation result of the patch's near field.

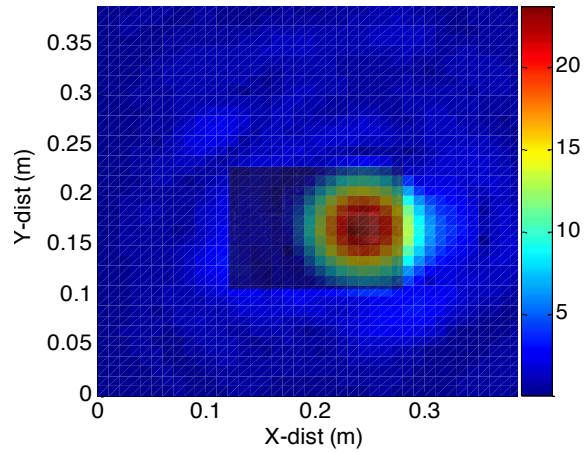


Fig. 7. Calculated focus fields (mV/m) at the source plane ($z=0\text{mm}$) with the scanned data acquired when the reference probe was placed near the patch.

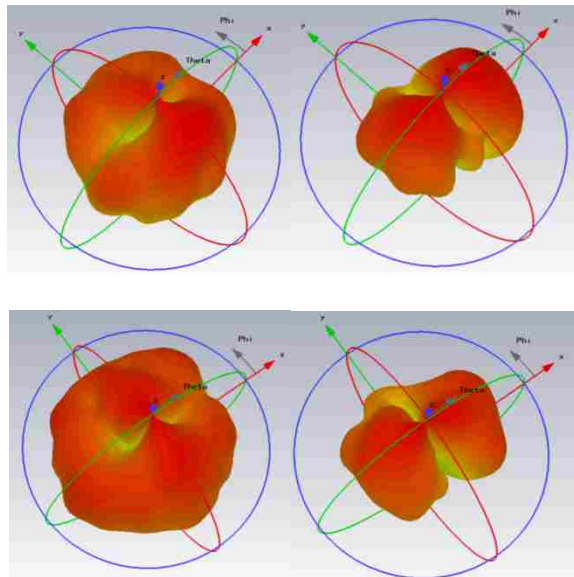


Fig. 8. The patch's far-field pattern. (top left) Θ_{theta} and (top right) Φ_{phi} calculated with the scanned data; (bottom left) Θ_{theta} and (bottom right) Φ_{phi} with CST simulation.

REFERENCES

- [1] A. D. Yaghjian, "An overview of near-field antenna measurements," *IEEE Transactions on Antennas and Propagation*, vol. 34, no. 1, pp. 30-45, Jan. 1986.

- [2] A. Ramanujan, Z. Riah, A. Louis, and B. Mazari, "Modeling the electromagnetic radiation of passive microwave components using a near-field scanning method," *IEEE Transactions on Electromagnetic Compatibility*, vol. 52, no. 4, pp. 1056-1059, Nov. 2010.
- [3] P. Maheshwari, V. Khilkevich, D. J. Pommerenke, H. Kajbaf, and J. Min, "Application of emission source microscopy technique to EMI source localization above 5 GHz," presented at the IEEE EMC Symposium, Raleigh, N.C., USA, 2014.
- [4] C. A. Balanis, *Advanced engineering electromagnetics*. vol. 20. New York: Wiley, 1989.
- [5] L. R. Arnaut, and C. S. Obiekezie, "Stochastic analysis of wideband near-field emissions from dipole antennas and integrated circuits," *IEEE Transactions on Electromagnetic Compatibility*, vol. 56, no. 1, pp. 93-101, Feb. 2014.
- [6] Matlab. [Online]. Available: <http://www.mathworks.com>
- [7] Agilent 4-port PNA-X Network Analyzer Data Sheet. Available: <http://cp.literature.agilent.com/litweb/pdf/N5245-90008.pdf>
- [8] J. J. Wang, "An examination of the theory and practices of planar near-field measurement," *IEEE Transactions on Antennas and Propagation*, vol. 36, no. 6, pp. 746-753, 1988.
- [9] J. R. Regué, M. Ribó, J. M. Garrell, and A. Martín, "A genetic algorithm based method for source identification and far-field radiated emissions prediction from near-field measurements for PCB characterization," *IEEE Transactions on Electromagnetic Compatibility*, vol. 43, no. 4, pp. 520-530, 2001.

- [10] T. K. Sarkar, and A. Taaghola, "Near-field to near/far-field transformation for arbitrary near-field geometry utilizing an equivalent electric current and MoM," *IEEE Transactions on Antennas and Propagation*, vol. 47, no. 3, pp. 566-573, 1999.
- [11] R. J. Luebbers, K. S. Kunz, M. Schneider, and F. Hunsberger, "A finite-difference time-domain near zone to far zone transformation," *IEEE Transactions on Antennas and Propagation*, vol. 39, no. 4, pp. 429-433, 1991.
- [12] CST Microwave studio. [Online]. Available: <http://www.cst.com>

II. Radio Frequency Interference Modeling of Complex Modules in Mobile Devices

Tianqi Li, *Student Member, IEEE*, Abhishek Patnaik, *Student Member, IEEE*,
Shubhankar Marathe, *Student Member, IEEE*, Giorgi Maghlakelidze, *Student Member, IEEE*, Victor Khilkevich, *Member, IEEE*, David J. Pommerenke, *Senior Member, IEEE*,

Abstract— Using Huygens’s Equivalent Theorem, a systematic approach based on scanned near fields for modeling radio frequency interference is introduced. Except for commercial code, the methodology does not require any additional mathematical algorithms, e.g., extracting dipole moments or reconstructing a source from the scanned data. The method can be applied to complex 3D noise structures. The effect of multiple scattering on the source and nearby obstacles is considered. The average over realization is applied to retrieve phase information from the random-like signal. As an application demonstration, an active cellphone LCD is modeled using phase-resolved near-field-scanned (NFS) data to calculate its radio frequency interference to the nearby antenna. Advantages and disadvantages of this method are discussed.

Index Terms—Cell phone, Electromagnetic compatibility (EMC), Interference, De-sense, Full-wave model, Liquid crystal display (LCD), Radio frequency interference (RFI), Near-field scan, Huygens’s Equivalence Theorem

I. INTRODUCTION

Intra-system electromagnetic compatibility (EMC), or radio-frequency interference (RFI), is a challenging problem in modern electronics [1]. For example, a mobile phone antenna and its receiver form an RF module that can detect signals as weak as -120dBm in a 200KHz bandwidth [2], if not disturbed by nearby electronics. However, the clock frequencies of a smart phone can reach GSM880, or in some cases, even GSM1800. The harmonics and data signals couple to the antenna and de-sensitize (de-sense) the RF system, thereby degrading the communication quality.

RFI modeling is necessary for optimizing the victim antenna design, location, grounding/shielding structures, and system floor planning at the early design phase. A noisy integrated circuit (IC) can be modeled directly if sufficient IC information exists [3]. However, in many practical cases, the noise source's internal information may be unknown, or if it is known, the source may be too complex to model. For example, given a cellphone RFI problem caused by a liquid crystal display (LCD), it is almost impossible to find the source mechanism at the microscopic level. An LCD panel may include more than 10 different material layers and have distributed and localized circuits (Fig. 1). It is unknown which traces/circuits constitute the RFI sources, what the source impedances are, or which structures would contribute to the coupling paths. In addition to its structural complexity, the module is behaviorally complex. An LCD may exhibit different RFI signatures when displaying different photos, and these signatures may appear as time-varying and stochastic.

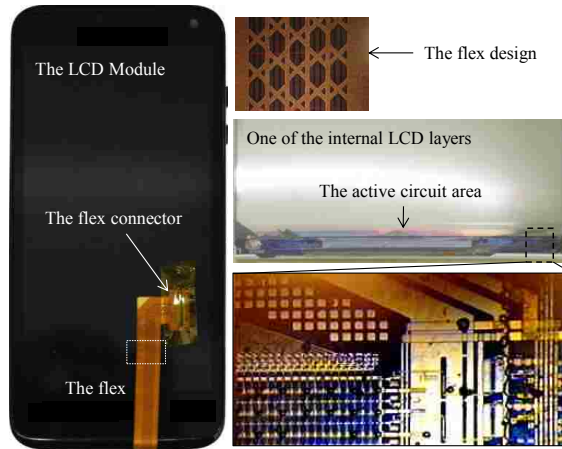


Fig. 1. An LCD's internal structure.

A solution to address the above challenge is to model a source with its near-field-scanned (NFS) data. This technique is based on the Surface Equivalence Theorem [4][5], which states that a source in a volume can be substituted with its emitted fields (as the impressed sources) imprinted onto the surface that encloses this volume. In [6]-[8], the impressed sources were calculated according to Huygens's Equivalence Principle from the NFS data.

Huygens's equivalence method in [6]-[8] has been applied mainly for far-field calculations; challenges may arise when modeling near-field problems. Wang applied Huygens's method and reciprocity to RFI modeling without considering the effect of multiple scattering [9]. However, within a compact mobile device, a noise source usually is surrounded by complex scatterers. Thus, if the noise source is substituted with its Huygens's equivalence, the scattering among the source and the nearby obstacles would not be taken into account, thereby yielding erroneous results. Franek et al. demonstrated such an error by placing an obstacle close to a Huygens's box [10]. To include the back-scattering, they refilled the Huygens's box with an approximation of the actual source structure.

In addition to Huygens's equivalence method, another solution category is the source reconstruction method, the core idea of which is that a source can be reconstructed by a matrix of electric and magnetic dipole moments. Usually, the operator provides the locations and types of sources, and the magnitude and phase are determined by matching fields to NFS data [11]-[18]. The source reconstruction method may be valuable for creating models for RFI coupling, if the following difficulties can be addressed adequately:

- Conveniently generate a unique and correct solution.
- Reconstruct the source from 3D NFS data, e.g., the scanned fields over a noisy camera module without a large reference plate nearby.
- Take the multiple scattering caused by 3D structures into consideration.

The most challenging part of both Huygens's equivalence method and the source reconstruction method is acquiring the NFS data of a complex structure. The measurement difficulties include the following:

- The fields can be extremely weak, resulting in a poor signal-to-noise ratio (SNR) on the scanned data.
- The noise is random or random-like, as it originates from switched power supplies in the phone, and thermal noise is added by the amplifier. Phase information should be retrieved from the random fields, which are correlated to the driving IC source overlaid with random noise.
- The scanning probe must be placed in the reactive field region of the device under test (DUT); otherwise, the evanescent modes that may contribute RFI will be lost. However, the probe should not change the source.

- A mobile device has a complex structure. Its antenna may share the same reference metal, usually the phone's body frame, with the noise source. Metal will inevitably pass through a Huygens's boundary.
- The scanning probe's positioning inaccuracy may introduce error.

In this paper, a systematic approach is proposed to model the RFI. This solution path combines Huygens's principle with correction for multiple scattering, sensitive resonant probes, reconstruction of the E-field from an H-field only scan, and the handling of random-like signals to form a novel method that allows the RFI coupling within a complex system to be modeled. We began our investigation by examining the rationale and then validated the method using numerical and experimental examples. To demonstrate the application of the proposed method, the coupling from an active LCD to the antenna within a cell phone was simulated and compared to measurements.

II. THE MODELING METHODOLOGY

A. Generalized RFI Modeling Workflow

According to the Induction Theorem [5], the fields of an arbitrary source and victim structure in free space can be considered as the superposition of three parts: 1) the emissions of the source (\vec{E}_1, \vec{H}_1) as they would be in the absence of the victim, 2) the scattered field caused by the presence of the victim structure (\vec{E}_s, \vec{H}_s), and 3) the re-scattered fields caused by the source structure ($\vec{E}_{ss}, \vec{H}_{ss}$), as shown in Fig. 2.

$$\begin{aligned}\vec{E} &= \vec{E}_1 + \vec{E}_S + \vec{E}_{SS} \\ \vec{H} &= \vec{H}_1 + \vec{H}_S + \vec{H}_{SS}\end{aligned}$$

ϵ, μ

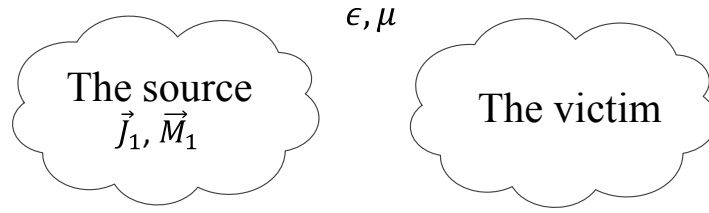
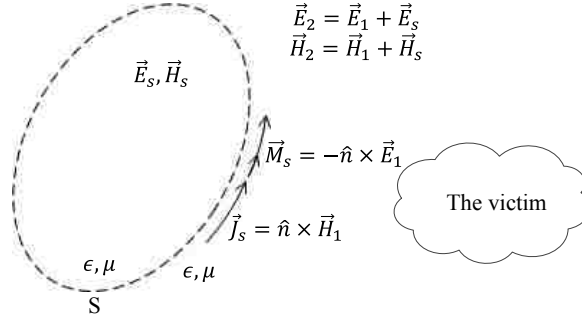


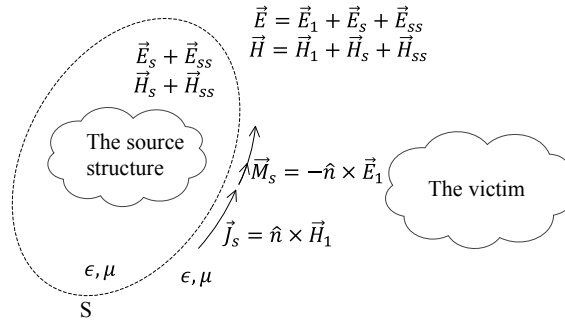
Fig. 2. An arbitrary source and a victim placed in space.

Outside a volume that contains the sources, the fields (\vec{E}_1, \vec{H}_1) can be obtained from the Surface Equivalent Theorem [4]. As shown in Fig. 2, an imaginary surface S (the Huygens's surface) was selected to enclose the sources. Only the region outside this Huygens's surface was of interest, so the fields inside S could have been any value. We assumed a void region inside S , while imprinting an impressed electric current source \vec{J}_S and a magnetic current source \vec{M}_S at this Huygens's surface. Due to the boundary condition over S , the fields (\vec{E}_1, \vec{H}_1) outside the Huygens's surface were recreated. This model was reduced further to the perfect magnetic conductor (PMC) equivalent model (Fig. 3c) [5], which only has an impressed source \vec{J}_S that exists over S and radiates due to the presence of the PMC, producing the original fields (\vec{E}_1, \vec{H}_1) outside the Huygens's surface.

Assuming that the volume is filled with PMC and then impressing \vec{J}_S on its surface S allows the total radiation (\vec{E}_1, \vec{H}_1) outside S to be recreated. Thus, only the tangential magnetic field needs to be scanned [19]. Alternatively, according to the Duality Theorem, one could also use the scanned electric field (E-field) and assume a perfect electric conductor (PEC) to recreate the (\vec{E}_1, \vec{H}_1) . However, according to the



(a)



(b)

Fig. 4. Models for solving the coupled noise into the victim: (a) without and (b) with the multiple-scattering effect.

The model in Fig. 4b shows the following valid boundary conditions over S ,

$$\vec{J}_s = \hat{n} \times (\vec{H} - \vec{H}_s - \vec{H}_{ss}) = \hat{n} \times \vec{H}_1 \quad (1)$$

$$\vec{M}_s = -\hat{n} \times (\vec{E} - \vec{E}_s - \vec{E}_{ss}) = -\hat{n} \times \vec{E}_1 \quad (2)$$

The scattered fields were generated by retaining both the source structure and the victim structure. Comparing this equivalent problem to the original problem (Fig. 2), the total field around the victim was the same, but the fields inside the Huygens's surface were different. Therefore, the limitation of this method is that the victim cannot be placed inside the Huygens's boundary.

The further multiple scattering between the source and the victim is automatically

included in the model shown in Fig. 4b. In addition, if other related scatters exist, they also may be included in the calculation domain to account for their effects.

The above analysis led to the general modeling work flow of a complex noise source, as shown in Fig. 5. Except for the test-related steps, the major modeling process can be conducted within CST microwave studio [21].

The proposed methodology is inevitably an approximate solution because the exact source geometry is usually unknown. Therefore, the re-scattered fields ($\vec{E}_{ss}, \vec{H}_{ss}$) cannot be exact.

B. A Metal Structure Passes through a Huygens's Boundary

In certain scenarios, the victim is electrically connected to the source structure, i.e., a metallic structure passes through the Huygens's surface S . In this case, the proposed methodology can be applied only when the source and the victim structures are unaltered after setting up the Huygens's boundaries. For example, as two microstrips reference the same ground plate (Fig. 6), the noise generated by the bottom strip can couple to the top trace because the ground has a limited size. In this case, the source's Huygens's box would unavoidably cut through the ground plate. The proposed Huygens's box 1 in Fig. 6 is valid, while the proposed box 2 is not. The structures enclosed by box 2 form an incomplete source structure, while the structures outside box 2 form an incomplete victim structure. Such a setup violates the previous analysis that the entire victim cannot be placed inside the Huygens's box. The proposed Huygens's box 1, however, does not have such a problem.

An advantage of using Huygens's box 1 is that the fields on the top surface can be approximated to 0. Thus, a model can be constructed simply by scanning the other 5

surfaces.

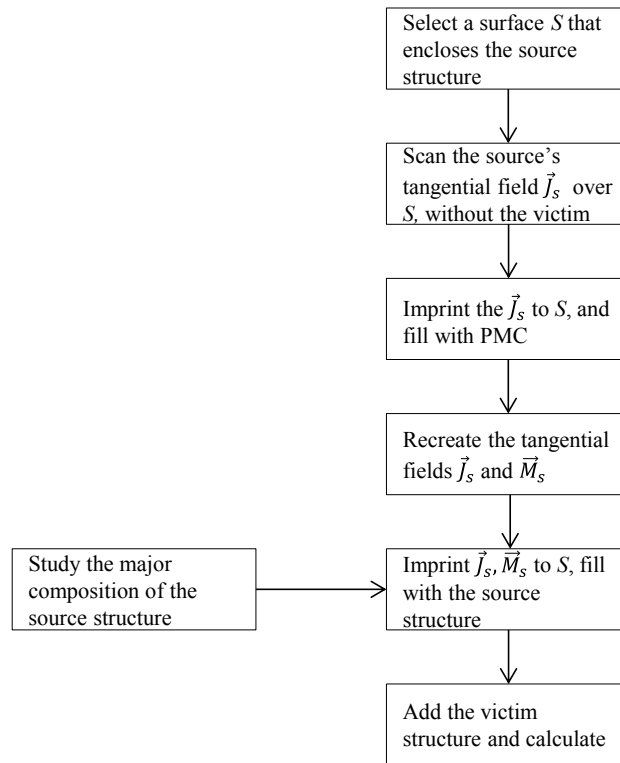


Fig. 5. Proposed RFI modeling work flow.

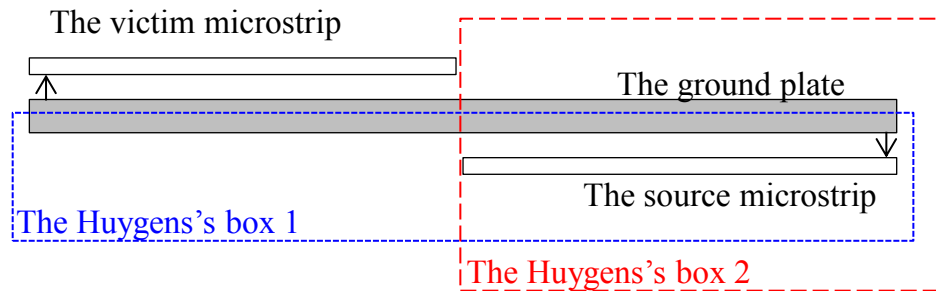


Fig. 6. Side view of two microstrips referencing the same ground plate that has a limited size. The proposed Huygens's box 2 is an invalid choice.

C. Testing the Tangential Fields over a Huygens's Surface

1) Utilizing a Resonant H-field Probe

A resonant type H-field probe [22] offers at least 5dB greater sensitivity at its

resonant frequency compared to a broadband loop probe of a similar size. This type of probe can be achieved by adding lumped components into a regular loop probe to make it resonant at a certain frequency. Therefore, such a probe is very suitable for testing weak fields within a narrow band. In this study, a 5mm x 5mm loop resonant at 900MHz, the dominant RFI frequency under interest, was selected as the scanning probe. Cooling the probe with liquid nitrogen could be another option to further increase the frontend SNR [23].

A resonant probe is prone to detuning if placed too close to a DUT. A probe's detuning property can be checked by measuring its return loss at different distances from the DUT. Accordingly, the Huygens's box boundary must be set where negligible change on the probe's return loss exists (S11).

In this study, a probing system was constructed with a 5mm H-field probe resonating at 900MHz, followed by an amplifier group consisting of ZX60-1215, ZFL-1000LN, and ZX60-33LN+ [24]. The amplifier ZX60-1215, with a 0.4dB noise figure, was used as the first stage to reduce the overall noise figure of the system.

The probing system was calibrated as a whole within an open stripline [25]. The calculated probing system factor equaled $(1.5+2.4i)\times 10^{-3}$ (A/m /V) at 904MHz.

2) *Two-Probe Setup for Scanning over Random Fields*

A cellphone in active mode exhibits modulated and time-varying noise fields that appear as random noises. To scan over the random-like fields and retrieve the phase information, the two-probe setup should be used for scanning [26]. Firstly, the reference probe location where strong LCD noise exists must be identified, and this local noise must have the same frequency and modulation pattern as the coupled noise in the primary

antenna. In this way, the reference noise is correlated to the noise that contributed to RFI. Assuming a scanning probe A and reference probe B, the phase of A can be retrieved from the averaged A/B test on a vector-network-analyzer set to tuned receiver mode [26][27].

III. METHODOLOGY VALIDATION

A. Numerical Validation

1) *The Victim and Source Share the Same Reference Plate*

A simple structure, as shown in Fig. 7, was constructed to validate the proposed RFI modeling procedure. Both the source and the victim shared the same plate as their reference. The top surface of the Huygens's box was selected such that it cut the plate into two pieces in the z direction. Thus, both the victim (outside the box) and the source (inside the box) remained almost unchanged. The tangential H fields over the Huygens's box were sampled with 2mm/step in both the x and y directions and 0.5mm/step in the z direction, with the victim structure removed. The fields at the z_{max} surface of the Huygens's box equaled 0, except for the slotted area. The tangential H fields were imprinted onto a PMC box, which was reconstructed by a dielectric box with a magnetic conductivity that equaled $5 \times 10^8/\text{Sm}$ (CST does not provide PMC material). Then, a new set of tangential E-fields and H-fields was captured. In CST, the E and H fields could not be recreated right at the Huygens's boundary where the original H-fields were imprinted. Instead, the recreated tangential fields had to be sampled at least one mesh cell away from the imprinted surface. Thus, the resulting Huygens's box (Fig. 8 top) was a bit larger than the previously proposed Huygens's box. The proposed methodology showed less than 1dB error compared to the direct model (Fig. 8).

B. Experimental Validation

1) Modeling of a Well-Defined Patch Structure

The goal of the experimental validation was to check the probing system and the entire modeling flow. With a well-defined patch structure excited by a well-defined signal (Fig. 9), the challenges caused by scanning the weak random fields can be excluded at this stage, and a direct model can be obtained easily to validate the entire workflow. The tangential fields of the five sides of the patch were scanned using the setup in Fig. 9, with the aid of the API's automatic scanning system [28]. The bottom side field was set to 0, as this surface was defined inside the bottom plate. The scanned tangential H-fields and the recreated E-field composed the Huygens's box model of this patch.

The 2mm-thick metal rod (yellow) sits on top of a slotted metal plate, which is regarded as the victim structure. Underneath this metal plate, a 0.5mm-thick L-shaped trace acts as the aggressor, with 1V excitation on one end. All the lumped elements (blue) are 50Ω load resistors. The proposed Huygens's box is framed with blue dashed lines. The victim structure was removed when sampling the source's Huygens's equivalent.

To validate this Huygens's box model, the fields at a different plane, e.g., E-fields at $z = 13.5\text{mm}$ plane, were calculated with the Huygens's model and compared with the direct model's result. The direct model was a full-wave model of the patch structure. The results shown in Fig. 10 illustrate that the fields on the Huygens's box were obtained and processed correctly.

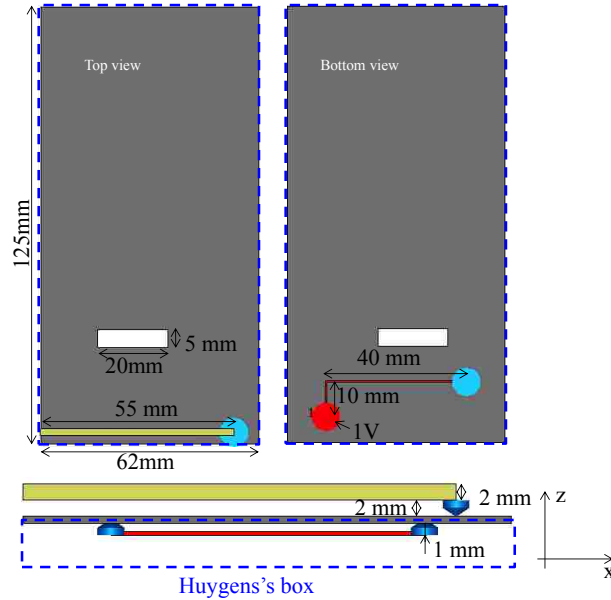


Fig. 7. The geometry created for numerically validating the proposed method.

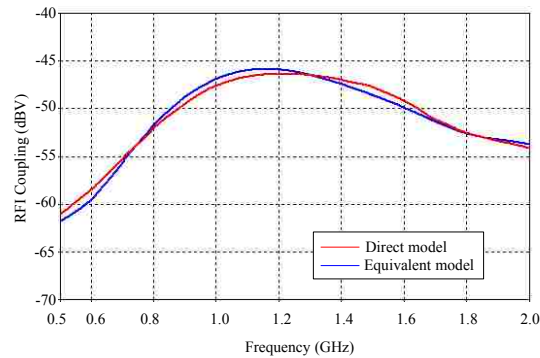


Fig. 8. The coupling result of Huygens's equivalent model compared to the direct model.

The coupled voltage is read on the 50Ω that terminates the victim rod.

Four monopoles (M1~M4) and four dipoles (D1~D4) were placed around the patch as the imagined victim antennas (Fig. 11). The proposed Huygens's model agreed with the direct model results within 3.5dB, except for the RFI at D1 and D3. They did not agree because the coupling to D1 and D3 were extremely low. The signal-to-noise ratio (SNR) of the scanned data was not high enough to cover such a large dynamic range, as the probe collected unwanted fields due to imperfect cross-polarization rejection. This

Huygens's model's dynamic range was approximately -40dB, which should be sufficient in RFI applications. To increase the dynamic range, one must build a probe that has a better rejection of unwanted field components.

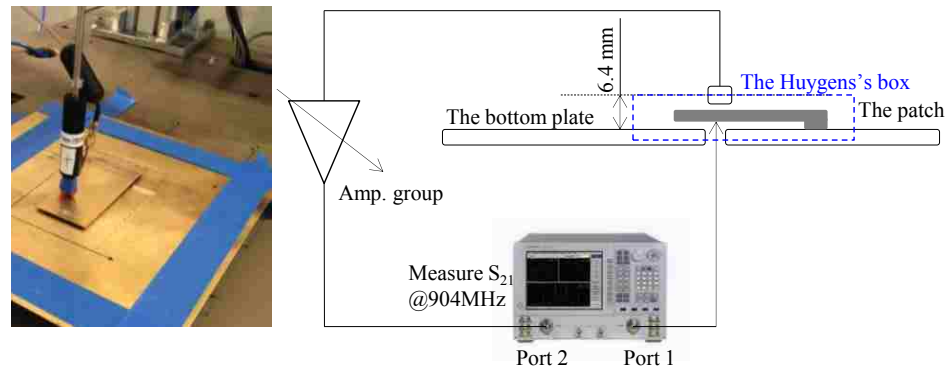


Fig. 9. Block diagram and layout of the phase-resolved scan over a 120mm×51mm patch. The patch was 2.9 mm above the bottom plate. It was excited at one end and shorted to the bottom plate at the other end. The structure was scanned at 2mm/step. The top surface tangential fields were sampled at 6.4 mm above the bottom plate.

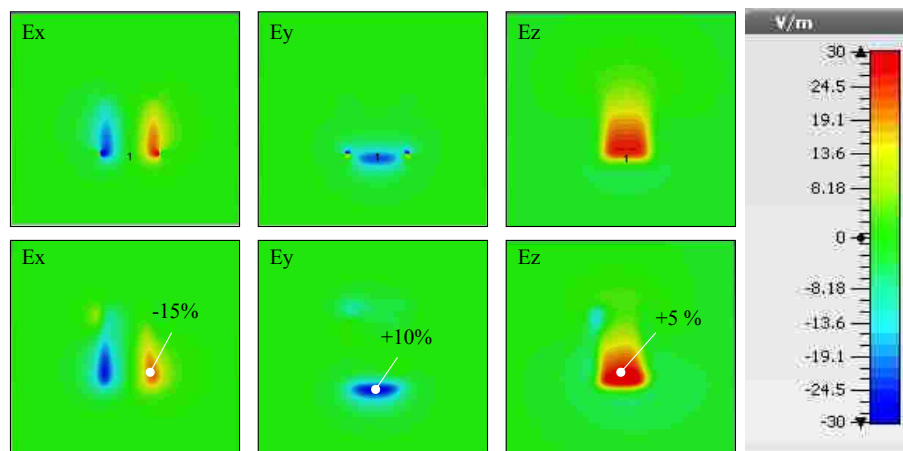


Fig. 10. Calculated real part of the E-field at 13.5 mm above the bottom plate at a given phase: (top row) direct model vs. (bottom row) the Huygens's box model. The differences in terms of percentage are marked.

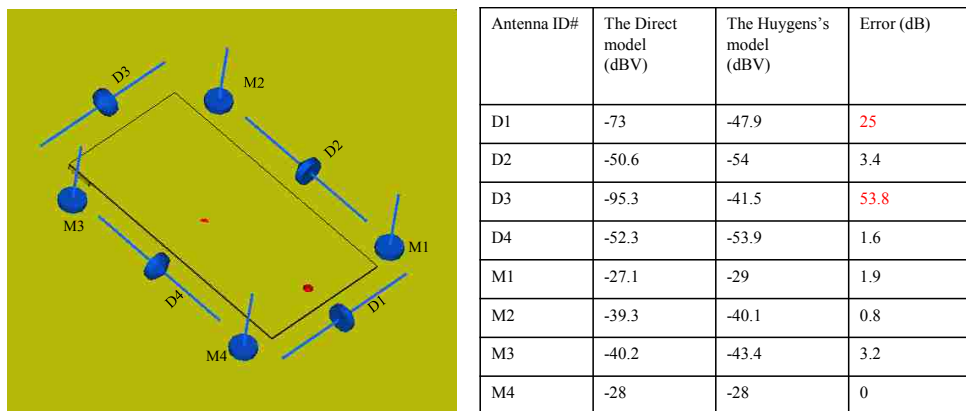


Fig. 11. Calculated RFI coupling to surrounding imaginary dipoles and monopoles. The direct model is compared to the Huygens's model. The patch was excited with 0 dBV.

2) Modeling of an LCD with a Well-Defined Excitation

The previous section explained the process of modeling a well-defined case. The next step in the validation of the methodology was to use an LCD in passive mode as the source. The LCD's internal electronics were not activated; instead, the LCD was driven by a signal generator so that the coupling from the LCD to a cell phone antenna could be tested without the complication of very weak and random signals, which is addressed in Section IV.

The passive LCD setup appears in Fig. 12. The victim antenna first was removed, and then the Huygens's model of the passive LCD was obtained in a way similar to that used when modeling the patch structure. The LCD was unpowered and excited by driving a power trace against the ground of the flex circuit that normally connects the LCD to the main board of the cell phone. The victim antenna then was added, and the S21 was used to judge the quality of the RFI prediction.

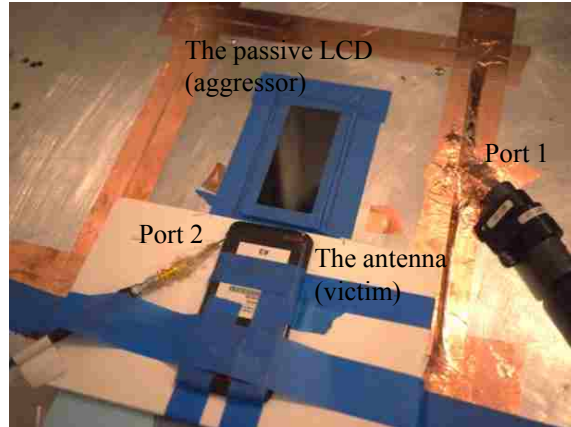


Fig. 12. Test setup for modeling a real LCD under passive mode. The LCD's flex was routed underneath the aluminum plate and directly grounded to this plate. A power trace on this flex was excited against the flex ground, where port 1 was defined. Port 2 was the victim antenna's port.

Predicting the coupling to the receiving antenna was the goal of the simulation, so the correctness of the model of the resonant receiving antenna had to be ensured. The antenna model was tested by comparing the calculated and measured return loss, as shown in Fig. 13. Then, the calculated RFI was compared to the tested result, as shown in Fig. 14. The difference between the calculated and measured result at 904MHz was 3dB.

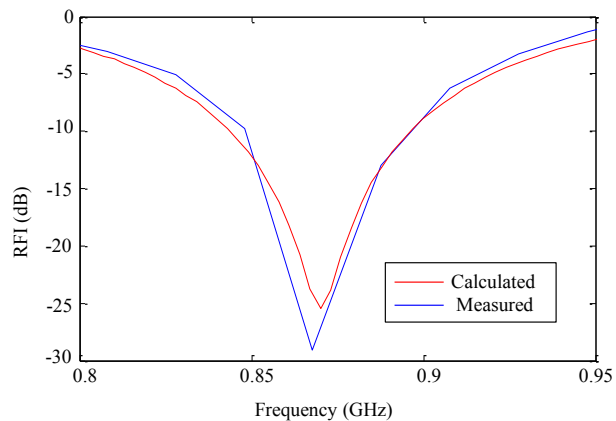


Fig. 13. Victim antenna's return loss, measured vs. simulated.

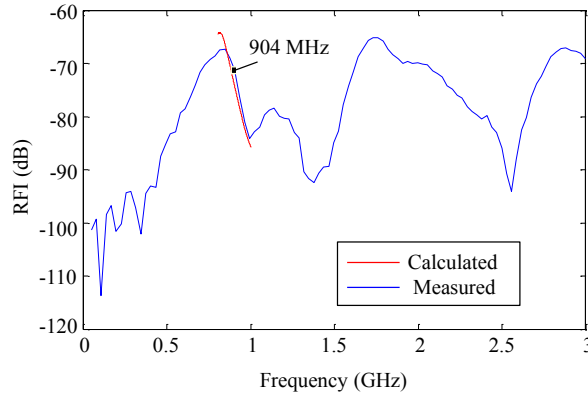


Fig. 14. RFI result of the setup shown in

Fig. 12, measured vs. calculated with the proposed Huygens's box model. Only the calculated result at 904MHz was exact because the Huygens's box was obtained at this frequency. The results at other frequencies were obtained by the extrapolation from 904MHz to adjacent frequencies with the same field data (performed by the CST engine).

IV. MODELING AN ACTIVE LCD IN A REAL CELL PHONE CONTEXT

A. Introduction to the Cell Phone under Investigation

A cell phone prototype showing RFI coupling from the LCD to its antenna was selected to validate the method. To measure the signal coupling to the antenna, the antenna was disconnected from the receiver and connected via a cable to a set of amplifiers. The phone was placed inside a shielding room to avoid coupling to the unwanted environmental RF signals (Fig. 15).

RFI noise was observed after turning the LCD on (Fig. 15). One of the dominant RFI frequencies, 903.76MHz, was selected to demonstrate the proposed modeling methodology.

The approximate cell phone geometry appears in Fig. 16. Preliminary near-field scanning identified two zones of high field strength at 903.76MHz. One zone was located

at the LCD flex connector, and the other was related to the active circuit region on the LCD panel. Analyzing the temporal variation of the field at these regions using zero span on a spectrum analyzer showed that the temporal variations at these regions were identical to the temporal variation of the signal at the antenna output. This indicates that these zones are related to RFI noise.

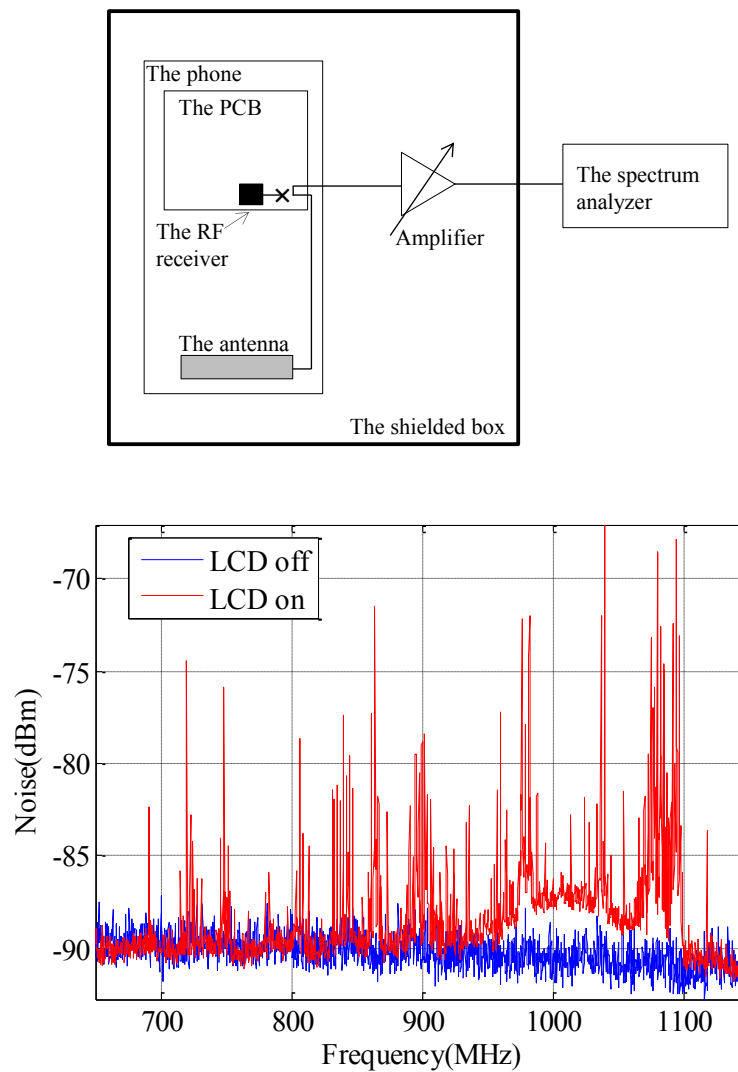


Fig. 15. (top) Test setup to check a phone's RFI, and (bottom) the tested RFI caused by the LCD operation; max hold was used, and RBW=2KHz. The data was un-calibrated.

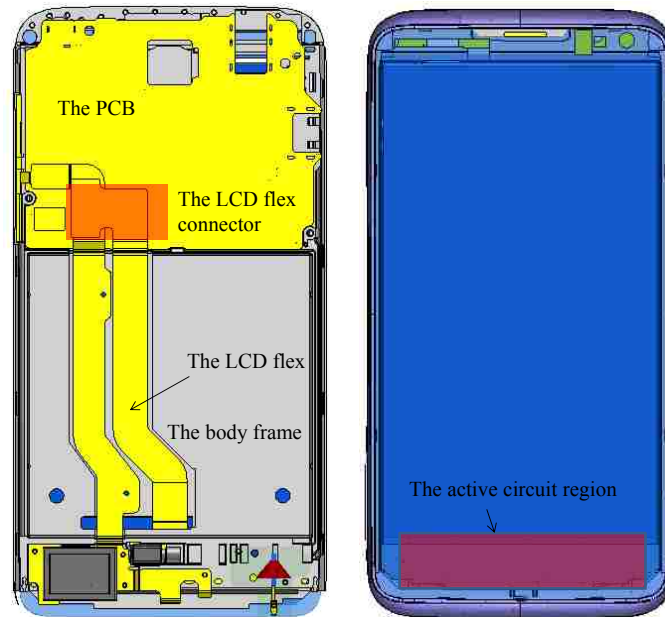


Fig. 16. Simplified cell phone structure: (left) backside view, without the back cover and battery, and (right) LCD-side view. The LCD is underneath the body frame, and its flex is routed on top of the body frame through a slot.

There are three possible sources of this RFI problem: the on-board interface IC that drives data into the LCD, the LCD's flex, and the LCD panel, where the active circuits are located. The LCD panel was found to be the dominant RFI source based on two observations; firstly, the LCD flex and the main PCB were totally shielded, while the resulting RFI did not change, and secondly, when a conductor was placed close to the LCD's active circuit area, the RFI changed significantly. This indicates that modeling the LCD's near field using a Huygens's box can predict the RFI coupling to the antenna for this cell phone.

B. Structure of the LCD

For the purpose of modeling the backscatter from the source region, the method requires refilling the Huygens's box with an approximate model of the source structure.

As the model cannot be created from the exact internal LCD structure, an approximate model had to be found. The LCD was comprised of multiple dielectric and conductive layers, such as the light spreader, the LCD structure, and the touch screen structure. The LCD and the touch screen structure contained metal. The LCD was approximated by a conductive layer of the same size as the outside dimensions of the LCD. To identify the effective conductivity of the major conductive layer, the LCD was placed on top of a copper plate, and its flex was routed on the other side of this plate (Fig. 17). The excitation port (port 1) was set between the flex ground and the copper plate. The same structure was built in CST. The LCD was modeled as a conductive plate with an unknown conductivity (σ). A value of $\sigma = 1000$ yielded a good match between the simulated and measured Z_{11} (Fig. 18).

C. Modeling the Active LCD with a Huygens's Box

The cell phone's LCD was scanned, as shown in Fig. 19. The cell phone was set in active mode and displayed a still picture. The reference probe's site was selected at the flex connector because the local field correlated strongly with the RFI noise at the antenna.

The system probe factor must be applied to the data captured by the VNA to convert the voltage into the magnitude and phase of the field strength. In this case, as only one RFI noise source existed, the mean ($|A|$) was taken as the field magnitude, and the angle [$\text{mean}(A/B)$] was taken as the phase. The averaged amplitudes were used to create the Huygens's box, so the model could only predict the average RFI at the same resolution bandwidth (RBW). To predict the RFI result in a different RBW, one must scale the scanned field magnitudes from one RBW to the desired RBW.



Fig. 17. (left) Bottom view and (mid) top view of the setup built for characterizing the LCD, and (right) full-wave model of this setup (the copper plate is hidden from view).

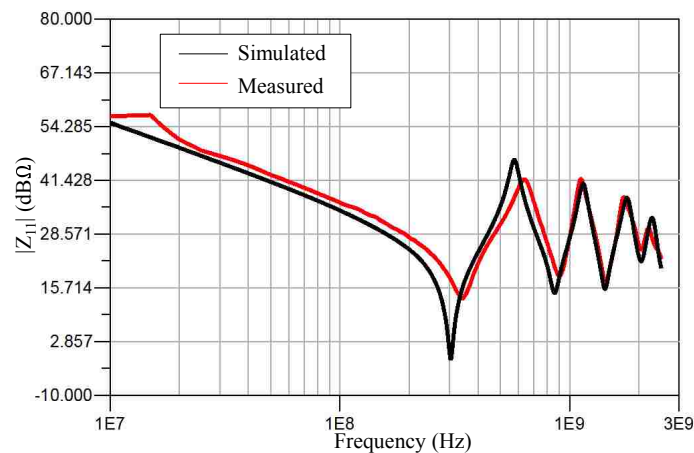


Fig. 18. Z_{11} of the Fig. 17 setup, when the LCD panel's $\sigma = 1000s/m$

The amplifier group 2, as illustrated in Fig. 19, ensures that the power levels of channel A and B are similar, as this maximizes the phase accuracy of the VNA [27].

Similar to Fig. 7, the proposed Huygens's box was selected such that it cut the body frame at $\frac{1}{2}$ of its thickness. Therefore, the bottom side field was set to 0 because the bottom side of the Huygens's box was inside the body frame.

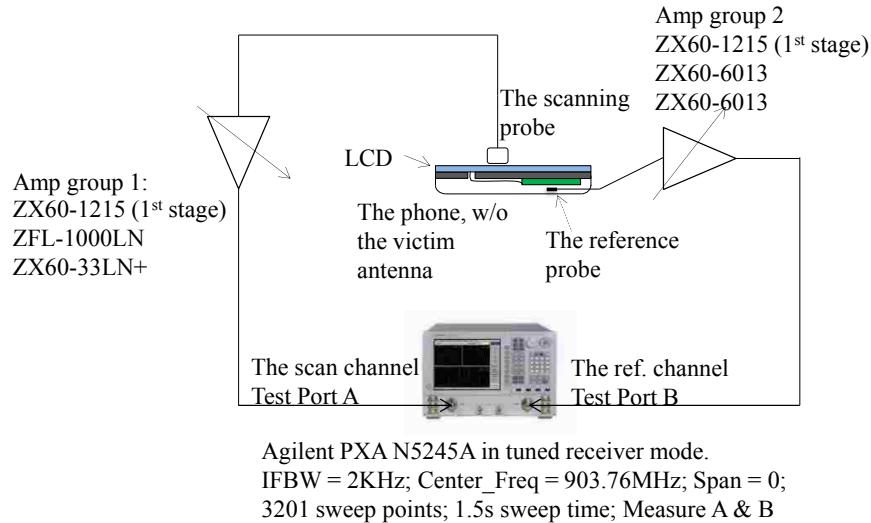


Fig. 19. Phase-resolving scanning setup for testing the active LCD. The top and side tangential H-fields of the LCD were measured. The reference probe was placed close to the LCD's flex connector, where strong correlated noise was captured.

The equivalent RFI model of an active LCD was built with the proposed workflow (Fig. 21). The Huygens's box was filled with the metallic bottom half of the body frame and the approximated LCD structure. The body frame and parts of the 2nd back cover were aluminum. The antenna, the PCB, and the flex circuits were modeled as copper. The plastic parts were approximated as dielectric material with $\epsilon_r=2$. No strong influence of the ϵ_r value on the calculated RFI results was observed, except when the ϵ_r was large enough to affect the antenna's resonant frequency. The top surface of the Huygens's box cut through the body frame, thereby imprinting it with the 0 field. The other five sides of this box were imprinted with measured and recreated data. The modeled RFI was $-3 \text{ dB}\mu\text{V}$, and the average test result was $-3.5 \text{ dB}\mu\text{V}$ at 903.76MHz . The measurement and simulation of the RFI coupling at 903.76 MHz matched within 1dB .

V. DISCUSSION

As long as the coupling was not very weak, the measurements and simulations differed by no more than 3.5 dB. This indicates that the method allows complex RFI coupling to be modeled. Unlike a full-wave solution, it does not require technical details and fine meshing of the source structure; the total calculation time is determined mainly by the complexity of the victim structure.

The refilled Huygens's box can be used as the RFI description of an LCD or other modules. This allows for the optimization of antenna structures and placement, and may be extended for use as a module qualification methodology without having to reveal proprietary details of the internal structure.

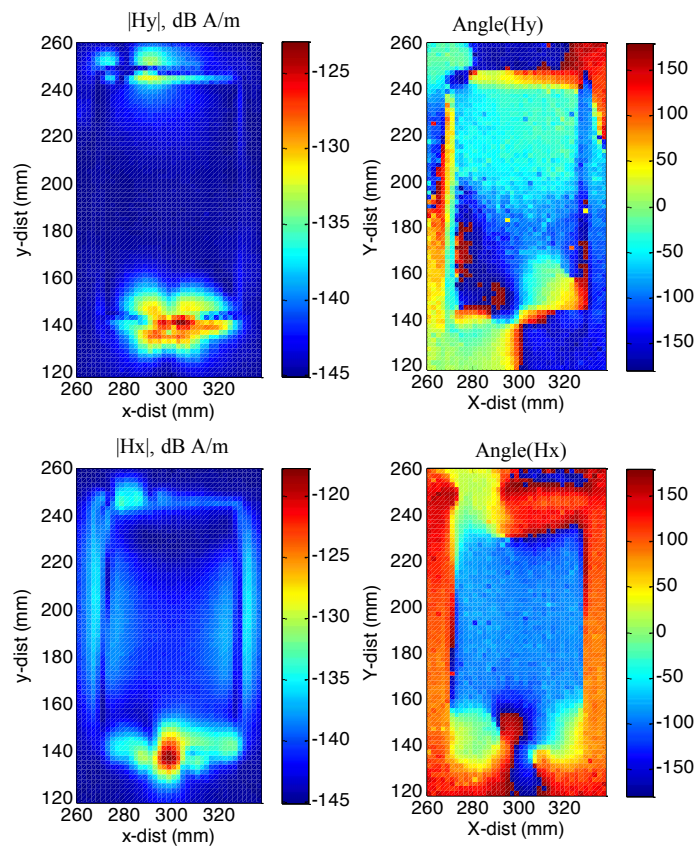


Fig. 20. Scanned tangential fields (H_x , H_y) at 903.76MHz at 3mm above the active LCD.

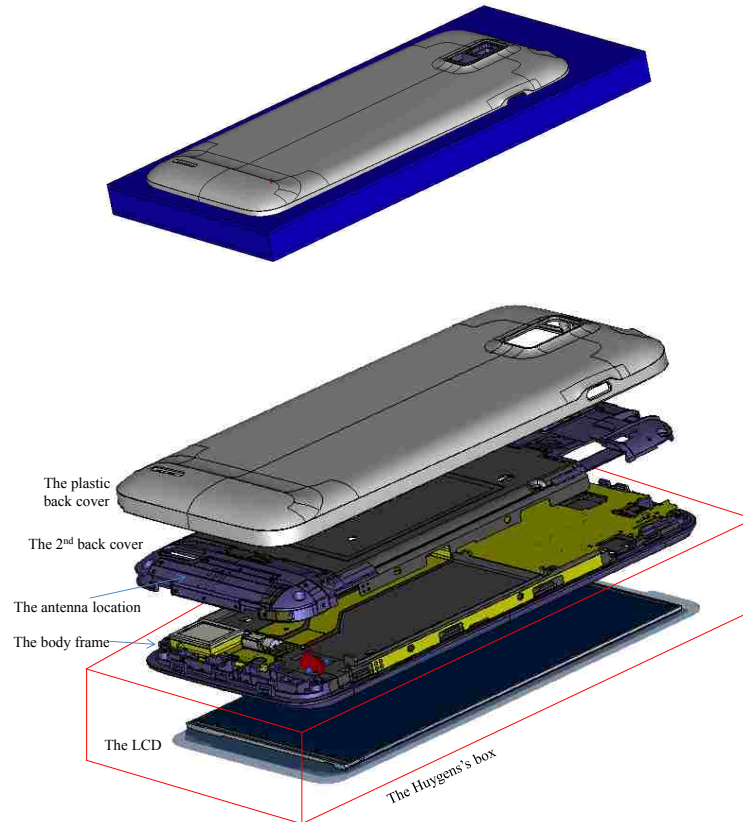


Fig. 21. (top) Complete cell phone RFI model, and (bottom) its internal details.

The difficulties of the method can be summarized as follows:

- The method requires phase-resolved scanning on random-like signals of very low amplitude.
- Knowledge of the potential (for module qualification) or actual (for analysis of a completed system) RFI source as the reference probe is required to measure this signal.
- If the Huygens's box cannot be placed such that it describes the source, it cannot be imported into different structures to predict coupling. Box 2 in Fig.6 illustrates such a case.

- A broadband analysis would be required to scan and numerically handle a large set of frequencies. In this case, the VNA-based phase-resolved measurement may need to be replaced by an oscilloscope-based method [29].

- The scan probe must reach all points on the Huygens's surface.

In spite of these difficulties, the results indicate that this method may open a path for RFI modeling and module qualification.

VI. CONCLUSION

An H-field-only Huygens's source-based methodology for modeling a complex noise-causing structure by its electromagnetic equivalence has been validated. The equivalence was enhanced to take nearby backscattering effects into account by refilling it with the approximate source structure geometry. It was demonstrated that the RFI coupling of an LCD to an antenna can be simulated. The model allows for antenna and system RF ground optimization.

REFERENCES

- [1] M. Ramdani, E. Sicard, A. Boyer, S. Ben Dhia, J. J. Whalen, T. H. Hubing, M. Coenen, and O. Wada, "The electromagnetic compatibility of integrated circuits—Past, present, and future," *IEEE Trans. Electromagn. Compat*, vol.51, no. 1, pp. 78-100, Feb. 2009.
- [2] K. Slattery, and H. Skinner, *Platform Interference in Wireless Systems: Models, Measurement, and Mitigation*. Burlington, MA, USA: Newns, 2008.
- [3] J. L. Levant, M. Ramdani, and R. Perdriau, "ICEM modelling of microcontroller current activity," *Microelectron. J.*, vol. 35, no. 6, pp. 501-507, Jun. 2004.

- [4] S. A. Schelkunoff, "Some equivalence theorems of electromagnetics and their application to radiation problems," *Bell System Technical J.* vol. 15, no. 1, pp. 92-112, 1936.
- [5] C. A. Balanis, *Advanced Engineering Electromagnetics*, Hoboken, NJ, USA: Wiley, 1989, pp. 323–325.
- [6] P. Peter, and T. K. Sarkar, "Planar near-field to far-field transformation using an equivalent magnetic current approach," *IEEE Trans. Antennas Propag.*, vol. 40, no.11, pp. 1348-1355, Nov. 1992.
- [7] H. Weng, D. G. Beetner, and R. E. DuBroff, "Prediction of radiated emissions using near-field measurements," *IEEE Trans. Electromagn. Compat.*, vol. 53, no. 4, pp. 891-899, Nov. 2011.
- [8] J. Shi, M. Cracraft, J. Zhang, R. E. DuBroff, and K. Slattery, "Using near-field scanning to predict radiated fields," in *Proc. IEEE Int. Symp. Electromagn. Compat.*, Santa Clara, CA, 2004, pp. 14-18.
- [9] H. Wang, V. Khilkevich, Y. J. Zhang, and J. Fan, "Estimating radio-frequency interference to an antenna due to near-field coupling using decomposition method based on reciprocity," *IEEE Trans. Electromagn. Compat.*, vol. 55, no. 6, pp. 1125-1131, 2013.
- [10] O. Franek, M. Sorensen, H. Ebert, and G. F. Pedersen, "Influence of nearby obstacles on the feasibility of a Huygens box as a field source," in *IEEE Int. Symp. Electromagn. Compat.*, pp. 600-604, 2012.
- [11] Z. Yu, J. A. Mix, S. Sajuyigbe, K. P. Slattery, and J. Fan, "An improved
- [12] dipole-moment model based on near-field scanning for characterizing

- [13] near-field coupling and far-field radiation from an IC," IEEE Trans. Electromagn. Compat., vol. 55, no. 1, pp. 97–108, 2013.
- [14] Z. Yu, J. A. Mix, S. S., K. P. Slattery, D. Pommerenke, and J. Fan, "Heat-sink modeling and design with dipole moments representing IC excitation," IEEE Trans. Electromagn. Compat. vol. 55, no. 1, pp. 168-174, 2013.
- [15] Z. Yu, J. Koo, J. A. Mix, K. Slattery, and J. Fan, "Extracting physical IC models using near-field scanning," in IEEE Int. Symp. Electromagn. Compat. pp. 317-320, 2010.
- [16] X. Tong, D.W.P. Thomas, A. Nothofer, P. Sewell, C. Christopoulos, "Modeling electromagnetic emissions from printed circuit boards in closed environments using equivalent dipoles," IEEE Trans. Electromagn. Compat, vol.52, no.2, pp.462-470, May 2010.
- [17] Y. Vives-Gilabert, C. Arcambal, A. Louis, F. de Daran, P. Eudeline, and B. Mazari, "Modeling magnetic radiations of electronic circuits using near-field scanning method," IEEE Trans. Electromagn. Compat, vol. 49, no. 2, pp. 391-400, 2007.
- [18] D. Baudry, C. Arcambal, A. Louis, B. Mazari, and P. Eudeline, "Applications of the near-field techniques in EMC investigations," IEEE Trans. Electromagn. Compat, vol. 49, no. 3, pp. 485-493, 2007.
- [19] X. Gao, J. Fan, Y. Zhang, H. Kajbaf, and D. Pommerenke, "Far-field prediction using only magnetic near-field scanning for EMI test," IEEE Trans. Electromagn. Compat, vol.PP, no.99, pp.1-9, May 2014.

- [20] A. E. H. Love, "The integration of the equations of propagation of electric waves," *Phil Trans. Roy. Soc. London, Ser. A*, vol. 197, pp. 1-45, 1901.
- [21] CST Microwave Studio. [Online]. Available: <http://www.cst.com>
- [22] H. Chuang, G. Li, E. Song, H. Park, H. T. Jang, H. B. Park, Y. J. Zhang, D. Pommerenke, T. L. Wu, J. Fan, "A magnetic-field resonant probe with enhanced sensitivity for RF interference applications," *IEEE Trans. Electromagn. Compat.*, vol.55, no.6, pp.991-998, Dec. 2013.
- [23] G. Li, W. Huang, and D. Pommerenke, "Effect of cooling on the probe system sensitivity for low signal strength RFI problems," in *IEEE Int. Symp. Electromagn. Compat.*, Denver, CO, 2013, pp. 134-137.
- [24] Minicircuits. [Online]. Available: <http://www.minicircuits.com>
- [25] M. L. Crawford, "Generation of standard EM fields using TEM transmission cells," *IEEE Trans. Electromagn. Compat.*, vol. 4, pp. 189-195, 1974.
- [26] T. Li and V. Kelkevich, "Phase resolved scan over multiple random noise sources," to be submitted to *IEEE Trans. on EMC*.
- [27] Agilent 4-port PNA-X Network Analyzer Data Sheet. Available: <http://cp.literature.agilent.com/litweb/pdf/N5245-90008.pdf>
- [28] Smart Scan EMI 350. [Online]. Available: <http://www.amberpi.com>
- [29] J. Zhang, K. W. Kam, J. Min, V. Khilkevich, D. Pommerenke, and J. Fan, "An effective method of probe calibration in phase-resolved near-field scanning for EMI application," *IEEE Trans. Inst. and Meas.*, vol.62, no.3, pp.648-658, March 2013.

III. System-Level Modeling for Transient Electrostatic-Discharge Simulation

Tianqi Li, *Student Member, IEEE*, Viswa Pillar, *Student Member, IEEE*, Zhen Li, *Student Member, IEEE*, Victor Khilkevich, *Member, IEEE*, David J. Pommerenke, *Senior Member, IEEE*, Junji Maeshima, *Member, IEEE*, Hideki Shumiya, *Member, IEEE*, Kenji Araki, *Senior Member, IEEE*

Abstract— This paper introduces an improved electrostatic discharge (ESD) system-level transient simulation modeling method and discusses its validation using IEC 61000-4-2 ESD pulses on a real-world product. The system model is composed of high current and broadband (up to 3GHz) models of R, L, C, ferrite beads, diodes, and integrated circuit IO pins. A complex return path model is the key to correctly modeling the system's response to the IEC excitation. The model includes energy-limited, time-dependent IC damage models. A power-time integral method is introduced to accurately determine if a junction would experience thermal runaway under an arbitrary injection waveform. The proposed method does not require knowledge of the junction's microscopic geometry, material information, defect location or melting temperature.

Index Terms— Electromagnetic compatibility (EMC), Electrostatic discharge (ESD), Human machine model (HMM), IEC 61000-4-2, System efficient ESD design (SEED), Transmission-line-pulser (TLP), Common mode

I. INTRODUCTION

Recent studies have shown that system-level electrostatic discharge (ESD) simulation can serve as a powerful tool for analyzing ESD performance [1]. The simulation enables the design of reliable protection on the first attempt and avoids the need for repeated design optimization tests.

The concept of ESD simulation has been promoted as an option in system-level ESD efficient design (SEED) [2]. SEED emphasizes the analysis of the interaction between the quasi-static I-V curve of a vulnerable pin and the pin's external protection. Gossner et al. applied SEED for analyzing an IO pin's response to ESD for different on-board protection solutions [3]. Monnereau et al. extended the modeling framework by adding trace and package models, and validated their method with an inverter circuit under a 100 ns transmission line pulser (TLP) excitation [4]. The authors of this paper previously published a hard error analysis of a cellphone's keyboard illumination circuit based on a 35ns TLP source [5].

Although the SEED simulation offers greatly improved system-level ESD design, some issues remain unresolved. Firstly, TLP-derived IC data show good repeatability due to the simplicity of the TLP waveform. However, the waveform does not resemble real ESD waveforms. To further optimize the design methodology, one should perform the characterization and simulation using the waveform described in IEC 61000-4-2 [6], or Human Machine Model (HMM) excitation for setting up the ESD simulation.

Even in cases in which a TLP-excited simulation can determine the circuit's reliability, such as in [4][5], it is still important to consider a circuit's response to IEC excitation for the following reasons: 1) TLP-based simulation results may be valid when

the damage is caused by the IEC's 2nd peak (residue portion), which has a long duration and can be mimicked by a TLP pulse. A TLP excitation does not reflect the consequences of the first few nanoseconds of an IEC excitation. 2) A TLP source is not suitable for modeling soft error, near field coupling or signal integrity (SI) problems caused by an ESD injection.

It is difficult to convert a TLP-based simulation into an IEC setup directly by substituting the TLP model with an ESD gun model. Compared to a TLP-based model, an IEC source-based setup requires more sophisticated modeling on the current return path in order to achieve an accurate circuit response under ESD tests. Furthermore, intensive use of flex-printed-circuits (FPCs) for connecting multiple PCBs creates complex return paths. Among the recent publications that researched system-level IEC simulation, some showed less accurate results compared to measurement, especially at the very first nanosecond, e.g., [7]. Some demonstrated excellent modeling results, but the investigated problems were only at the circuit-board level rather than the real product level due to the lack of complex return path structures, e.g., [8] [9].

In addition to modeling the PCB-based and IC internal ESD protection structures, a failure criterion is needed. Using only a TLP-derived constant failure current threshold [10] may be insufficient if this threshold is only surpassed for a few nanoseconds. This will be the case if the initial peak of the ESD current surpasses the threshold but the second peak remains below it. As Notermans et al. concluded after characterizing the ESD failure of ggMOSFET, "For a real system, dynamic failure must be taken into account as well" [12]. Particularly, it will be shown later in this paper that a complex network could introduce an oscillatory current waveform inside the system, thereby

making a constant current threshold inapplicable.

In the study presented in this paper, we modeled a cell phone circuit in realistic IEC testing scenarios. The state of the art of this paper includes the following four parts. Firstly, typical components (R, L, C, ferrite beads, and semiconductor devices) under high current and high frequency excitations are modeled. Secondly, a detailed model of the complex return path inside the phone is presented. Thirdly, a time-dependent destruction model is presented for the analysis of a semiconductor's hard failures. Finally, a power-time integral method is introduced to accurately determine if a junction would suffer thermal damage under an arbitrary injection waveform.

The remainder of this paper is organized as follows. Section II describes the product under investigation. The test systems and methods for creating the model are introduced in Section III. The component models are shown in Section IV. Section IV presents the semiconductor's failure model and discusses the development of the thermal runaway criterion of a junction under an arbitrary waveform. Section VI mainly discusses the ESD gun model and common-mode path modeling. Section VII shows the validation of the system-level model and the model's application for hard error analysis.

II. SYSTEM UNDER INVESTIGATION

A vulnerable keypad backlight LED circuit in a smart phone, as shown in Fig. 1, was investigated. The driver IC controlled the LED's brightness by varying the IO pin's state. All component information will be kept confidential because of intellectual property constraints. ESD tests indicated that the LED was a sensitive zapping point. During product-level tests, air-mode discharge sometimes struck through the aperture between the plastic buttons that covered the LED, and coupled into the illumination

circuits.

At first glance, the circuit's behavior under ESD appeared somewhat complex for the following reasons: 1) L-C pairs could cause resonance; 2) ferrite beads and capacitors may saturate or show nonlinear behavior under high current injection; and 3) the keyboard PCB was connected to the main PCB through an FPC, which introduced a complex return path for the ESD current.

III. MODELING METHODOLOGY

A component model was created based on an RF model and a device model obtained under high current, as shown in Fig. 2. This combination ensures sufficient accuracy under IEC 61000-4-2 or HMM excitations. Based on the 0.7-1ns rise time and the response of nonlinear elements, a modeling bandwidth of 3 GHz was selected. Z-parameters were used to obtain the RF model.

The high-current I-V curves were extracted using a 15~40 ns adjustable TLP pulse (Fig. 3). To control the parasitics of the test setup, inductances were minimized, e.g., a circular arrangement of five 10-Ohm resistors was used to create a broadband 2-Ohm current measurement shunt.

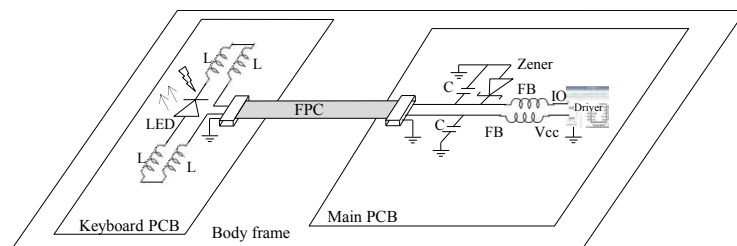


Fig. 1. The layout of the cell phone's keyboard backlight circuit. FB here stands for ferrite bead. The LED's cathode was selected as the entry point during product-level ESD testing. Both the LED and the Driver IC were considered vulnerable parts.

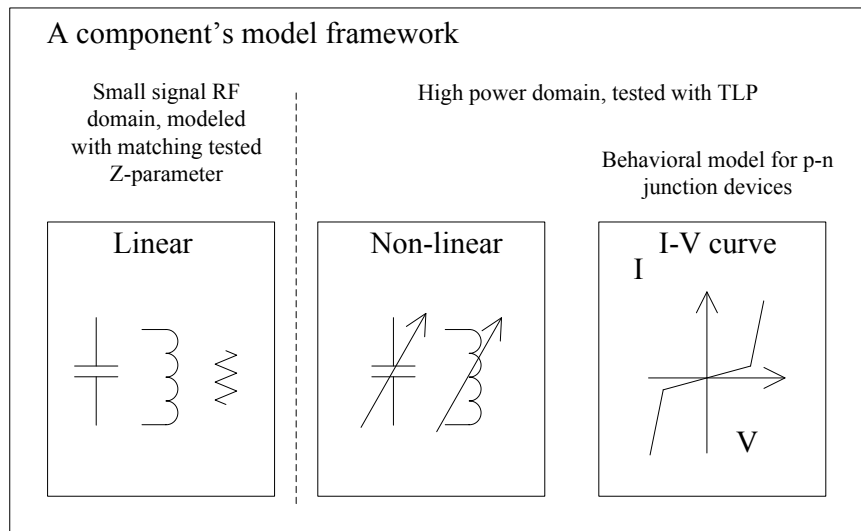


Fig. 2. Complete modeling framework for every device.

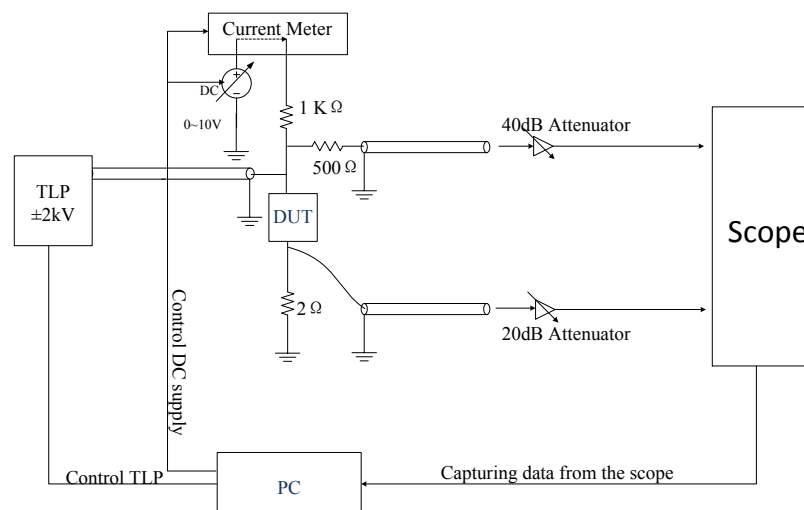


Fig. 3. One of the automatic TLP systems used to capture the voltage and current pulse of a DUT. Devices with multiple pins have been tested using a TDR-TLP similar to the one used in [14]. In this study, the current meter and adjustable DC power source were used to record the low-voltage static I-V curve and to check the DUT for damage.

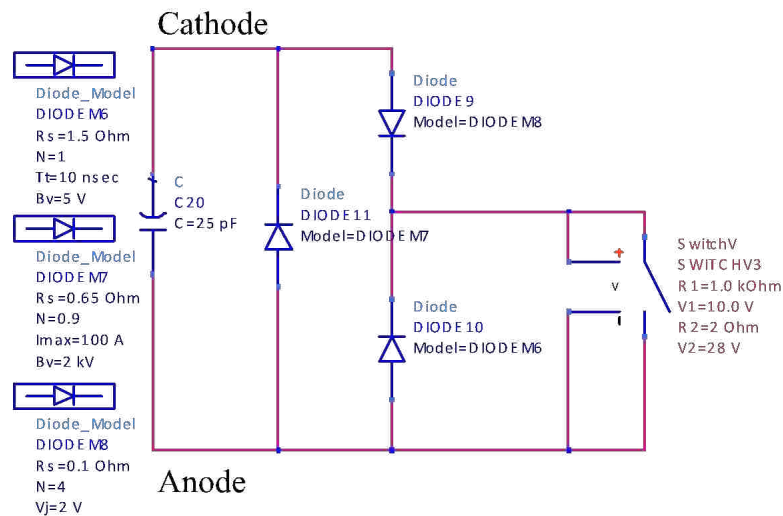
IV. COMPONENT MODELS

A. Semiconductor devices

Similar measurements were used to determine the VI behavior of LEDs, Zener diodes and IC pins. The only difference was that the IC was powered to ensure the same operating conditions as those encountered during system-level testing.

The Zener diode's transient I-V curve appears in Fig. 4, as does a behavioral model developed by fitting this curve. Diode 11 defined the I-V characteristics of the Zener diode under negative pulses applied to its cathode; diode 10 and the switch (actually, a voltage controlled resistor) determined the positive I-V characteristics. Diode 9 was used as a unidirectional switch to separate the positive and negative pulse injections.

The capacitance of the Zener diode was measured using a vector-network analyzer (VNA). Due to its large value of 25pF, it was determined that the diode would carry most of the current during the first nanoseconds of the ESD pulse.



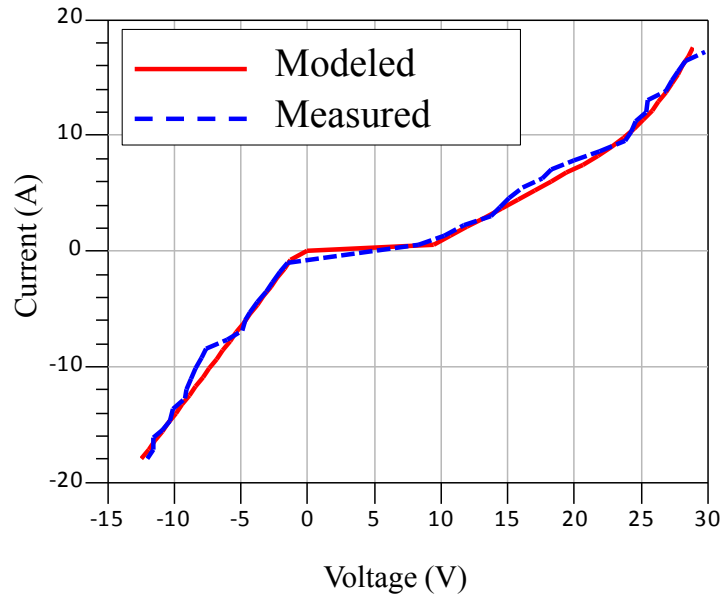
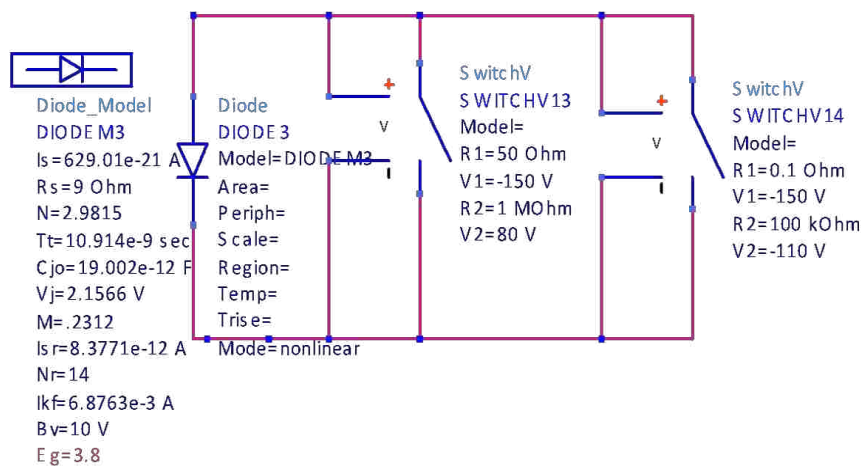


Fig. 4. (top) Model of the Zener diode, and (bottom) transient I-V characteristics of the Zener diode, simulated vs. measured.

The LED model (Fig. 5) is based on a similar concept. It has two parts: the factory-provided SPICE model for nominal current conditions, and two voltage-controlled resistances to mimic the high current I-V behavior. The factory model already included the capacitance, so no external RF model is needed here.



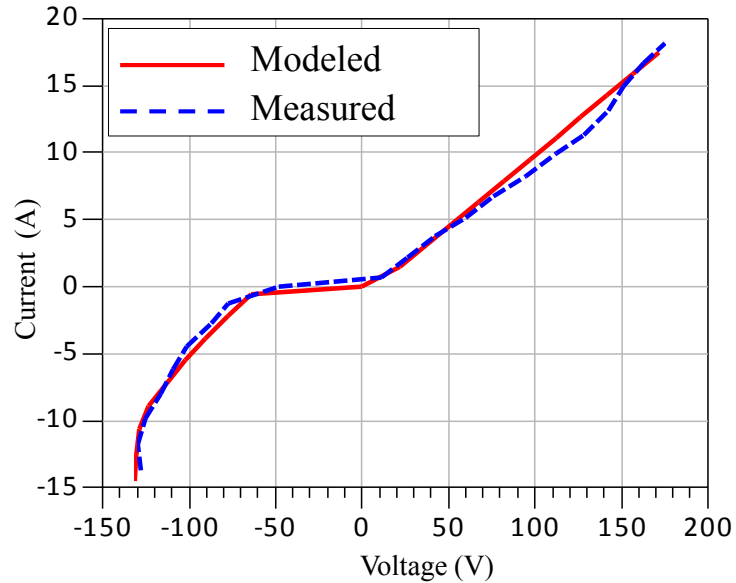
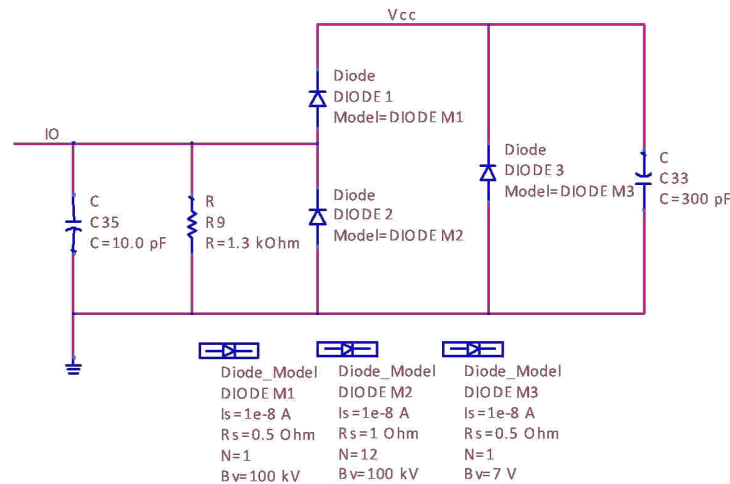
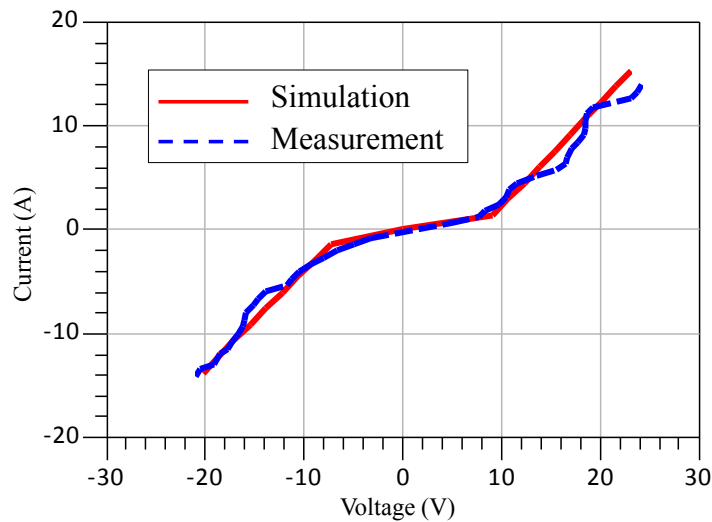


Fig. 5. (top) LED model and (bottom) its I/V curve.

The IO pin on the driver IC was modeled as a three-terminal device. Firstly, A TLP was used to obtain the power clamp of the Vcc network (Diode 3 in Fig. 6). Then, the high-side (DIODE1) and low-side (DIODE2) protection diodes of the IO pin were measured by applying positive and negative pulses to the IO pin, respectively. Finally, using a VNA, the values of the linear components (C, R and C33) were derived. The 300pF power rail capacitor is a combination of junction, gate and metallization capacitance. The system contains a large 2uF on-board capacitor placed in parallel.



(a)



(b)

Fig. 6. (a) IO pin model and (b) transient I-V characteristics of the IO pin, simulated vs. measured.

B. Capacitors, Ferrite Beads and Inductors

The voltage across a capacitor may lead to sparking, capacitor breakdown and a recoverable change in the capacitance value [15][16]. Fig. 7 shows the voltage and

current of a 10V-rated 10 nF X7R capacitor that was excited with a 15ns 3kV TLP.

Although the charge current was constant, a nonlinear voltage increase occurred. This indicates that the capacitance decreased as the voltage increased. The capacitance variation over time, or $C(t)$, can be calculated from the measured voltage and charging current waveform,

$$C(t) = \frac{I(t)}{dV(t)/dt} \quad (1)$$

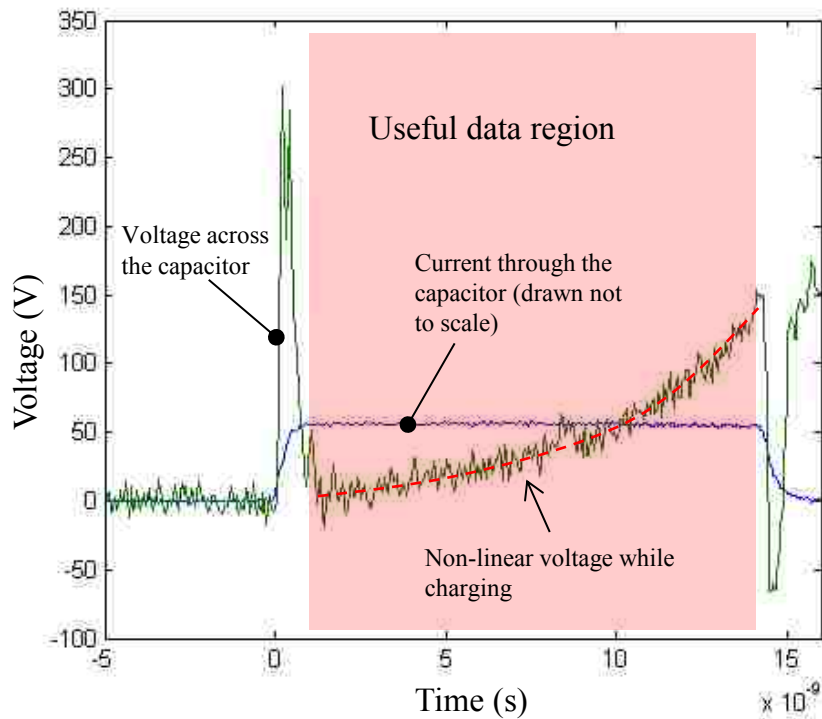


Fig. 7. Voltage and current of a 10V-rated X7R 10nF capacitor excited by a 15ns wide TLP pulse at 3kV charge voltage. Parasitic inductances in the measurement setup caused the initial voltage peak. After the peak, a nonlinear voltage increase occurred, although the current remained constant.

The C-V behavior was approximated by an arc-tangent function (2) to account for this C-V behavior, although other researchers have shown that quartic functions can work equally well [17].

$$C_{\text{model}} = -\tan^{-1}\left(\frac{|V|}{A} - B\right) \times C + D \quad (2)$$

where A-D tune the model, as shown in Fig. 8. For this specific capacitor, the best match was achieved at $A=18$, $B=2.2$, $C=2.8$ and $D=7$

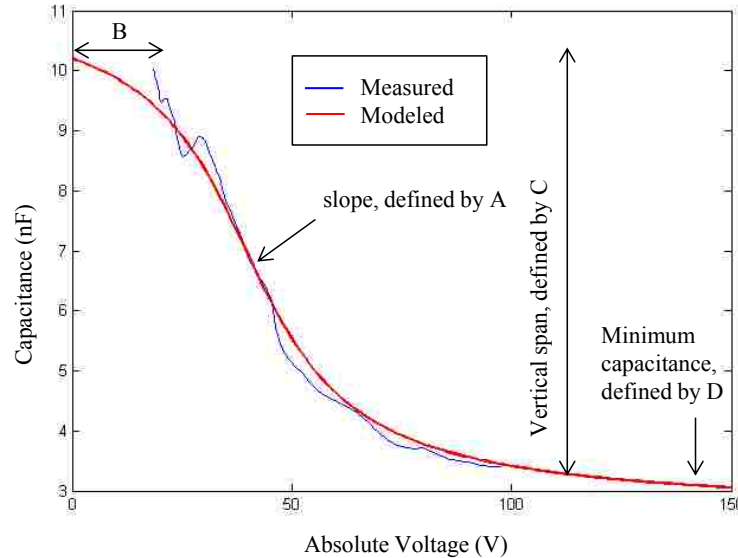


Fig. 8. Capacitance-voltage nonlinear relation, $C(V)$, of the 10V-rated 10nF X7R capacitor, simulated vs. measured.

Using the arc-tangent function, together with equivalent-series-resistance (ESR) and equivalent-series-inductance (ESL) obtained from measured Z-parameters, a complete capacitor model can be created in Agilent's Advanced Design System [18].

Not all capacitors behave nonlinearly under ESD. The low dielectric constant of NP0 ceramic will show little or no non linearity; however, the low capacitance values

achievable with small-package NP0 capacitors may spark over.

Similar to capacitors, ferrites may exhibit saturation or other nonlinear behavior under high current conditions. The nonlinear inductance can be approximated using the following equation:

$$L(t) = \frac{V(t)}{dI(t)/dt} \quad (3)$$

In certain cases, the additional high-frequency noise on the measured $I(t)$ may cause dI/dt to change significantly, thereby interfering with the calculated $L(t)$. To calculate the $L(t)$, one could either perform low-pass filtering on the tested raw data, or use $\frac{\int V(t)dt}{I(t)}$ to calculate.

The inductance-current relationship can be modeled by a nonlinear arc-tangent function, as used in capacitor modeling. Here, we used an alternative method, a quartic equation, for modeling.

$$L_{\text{model}} = L_{\text{sat}} + \frac{L_0 - L_{\text{sat}}}{1 + AI^2 + BI^4} \quad (4)$$

where I stands for the current flow through the nonlinear inductor; L_0 is the initial/nominal inductance; and L_{sat} represents the saturated inductance. $A=2$ and $B=1$ for the specific ferrite we tested. Fig. 9 shows the modeled curve of a ferrite with an equivalent 60nH inductance that can be saturated to 20nH.

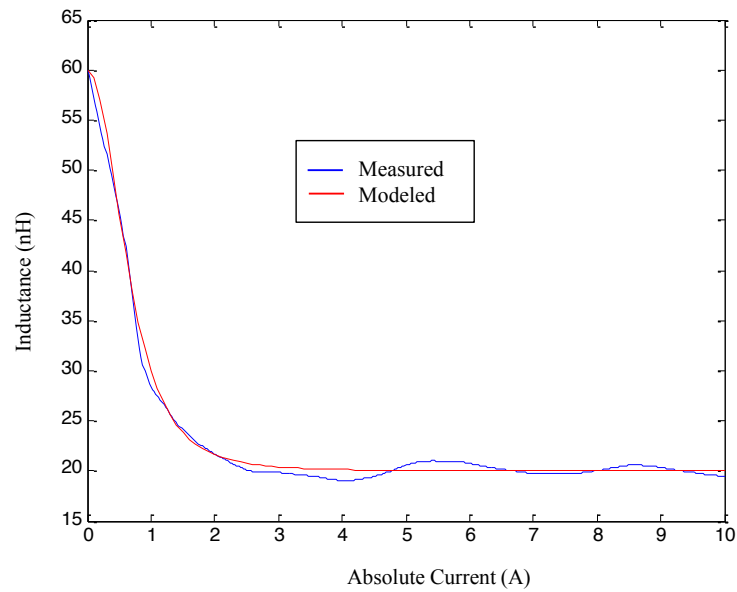


Fig. 9. Inductance as a function of current defined using Eq. (4).

The complete model of the ferrite appears in Fig. 10. Besides the nonlinear inductance model (SDD1P), other linear models can express the effect of the capacitance and loss following Yu's topology [19]. These linear parts usually can be found in a device's datasheet and can be checked by measuring the S-parameters. This model does not take hysteresis into account because the ferrite bead uses soft magnetic materials that exhibit no relevant hysteresis [20].

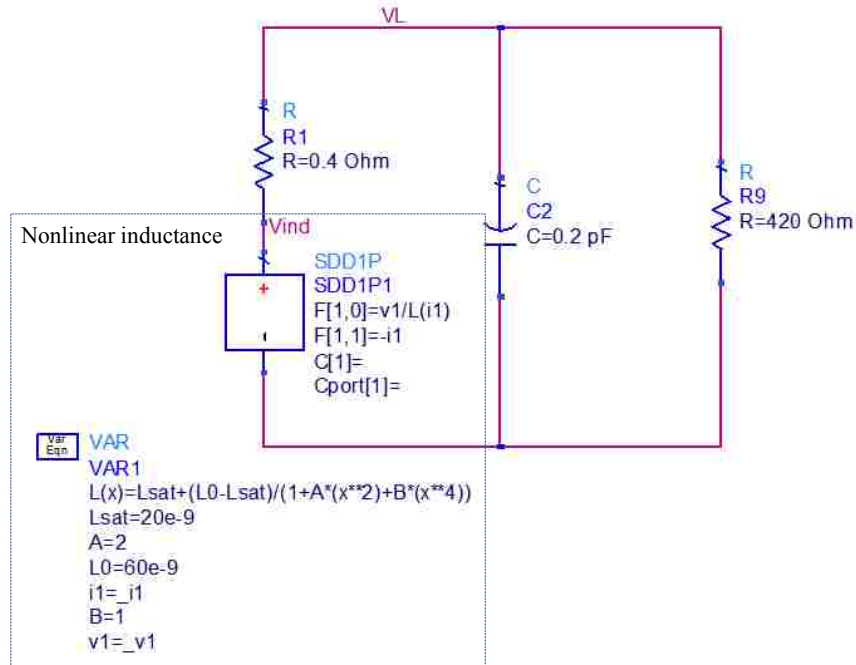


Fig. 10. Nonlinear model of a ferrite bead.

V. DYNAMIC DESTRUCTION THRESHOLD MODELING

A. Failure Power Models

To determine if a specific ESD will damage a device, its robustness threshold must be known. As discussed previously, a simple current threshold may not be sufficient; a dynamic threshold will better predict complex waveforms, such as an HMM discharge. Using a TLP with a varying pulse width, the damage threshold function (Fig. 11) was created. The TLP current decreased as the pulse length increased, indicating that the device was energy limited.

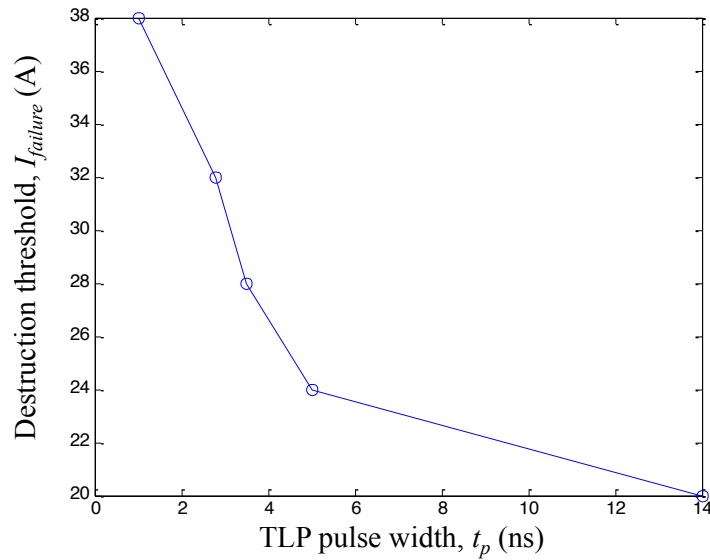


Fig. 11. Tested time-dependent damage threshold of the driver IC in terms of its through current.

Semiconductor devices under electrical over stress (EOS) have many microscopic failure mechanisms, e.g., surface breakdown around a junction and internal body breakdown through a junction. However, as Wunsch noted in [21], most failure mechanisms are linked primarily to the junction temperature. The widely used junction thermal model was developed by Wunsch and Bell [21], and later, Taska [22]. Their thermal analysis yielded the failure power (P) per unit junction area (A) as a function of the rectangular pulse width (t_p):

$$\frac{P}{A} = K_1 t_p^{-1} + K_2 t_p^{-1/2} + K \quad (5)$$

where K_1 , K_2 and K are design-specific parameters that relate to the junction material and conductivities. The resulting curve of (5) appears in Fig. 12.

The parameters K_1 , K_2 and K may not always be derived explicitly from junction design because in many applications, the material information and junction geometries

are not known. They can be determined, however, by fitting the measured curves, as shown in Fig. 13 and Fig. 14.

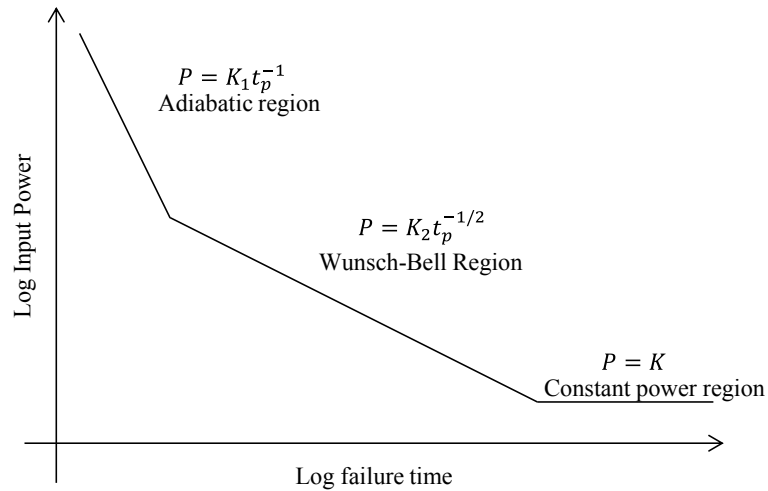


Fig. 12. Junction damage power versus rectangular pulse width [23].

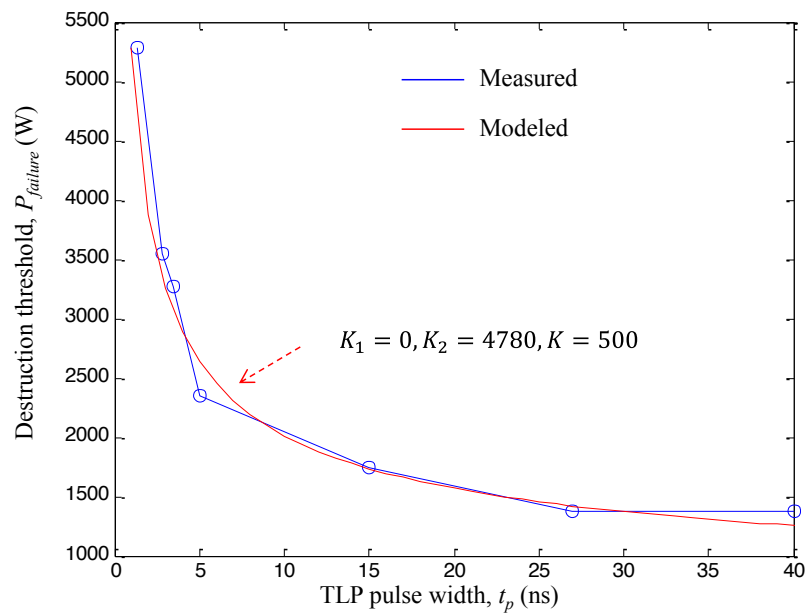


Fig. 13. Time-dependent damage threshold of the InGaN white LED in terms of its injection power, measured vs. modeled.

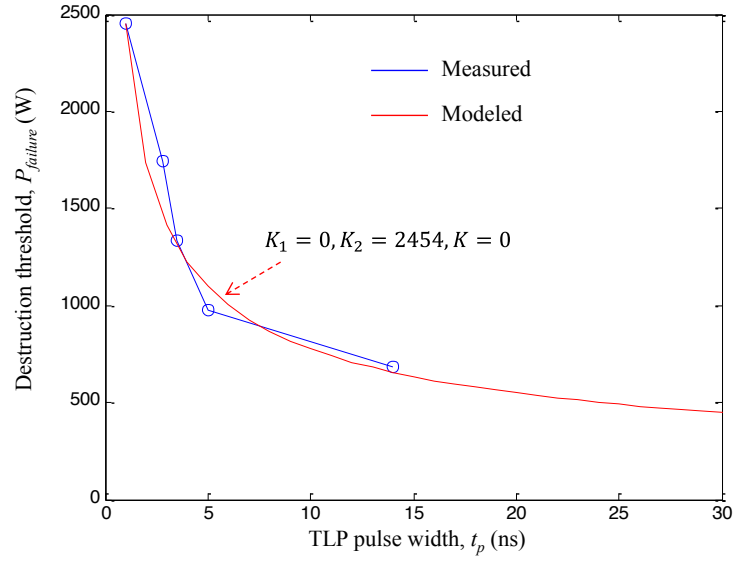


Fig. 14. Time-dependent damage threshold of the LED driver's IO pin in terms of its injection power, measured vs. modeled.

B. Failure Criteria

To determine device failure under time-varying waveform $P(\tau)$ based on the knowledge of the TLP tested failure power/time relationship $P_0(t)$, one can identify whether or not any portion in $P(\tau)$ injected the same amount of energy as a certain destructive rectangular pulse.

This idea can be derived from heat transfer equation [24] :

$$\frac{\partial T}{\partial t} - D\nabla^2 T = \frac{q(t)}{\rho C_p} \quad (6)$$

where T is the junction temperature, ρ is the density, C_p is the specific heat capacity, D is the thermal diffusivity and $q(t)$ is the heating rate per unit volume. The Green's function, or the solution to this function, is:

$$\frac{\partial G}{\partial t} - D\nabla^2 G = \delta(r - r')\delta(t - \tau) \quad (7)$$

The Green's function is known as the impulse response in both the time and spatial domains. As an injection source $P(r', \tau)$ heating a defect volume Δ , the temperature at an observation location r (the vulnerable point) at time t can be written as [25]:

$$T(r, t) = T_0 + \int_0^t \frac{P(\tau)}{\rho c_p \Delta} d\tau \int_{\Delta} G(r, t, r', \tau) dr' \quad (8)$$

where T_0 is the initial ambient temperature.

A rectangular pulse with an amplitude of P_0 and a duration of t_f can damage a semiconductor junction because the failure point temperature reaches the failure temperature T_c :

$$T_c = T_0 + P_0 \int_0^{t_f} \frac{1}{\rho c_p \Delta} d\tau \int_{\Delta} G(r, t, r', \tau) dr' \quad (9)$$

If an arbitrary injection profile that starts at an arbitrary time τ_0 can also generate the same amount of heat within a duration of t_f :

$$T_c = T_0 + \int_{\tau_0}^{\tau_0+t_f} \frac{P(\tau)}{\rho c_p \Delta} d\tau \int_{\Delta} G(r, t, r', \tau) dr' \quad (10)$$

this arbitrary waveform can be considered destructive. Therefore, the heat contribution of this arbitrary waveform to its equivalent rectangular pulse can be related as:

$$\int_{\tau_0}^{\tau_0+t_f} P(\tau) d\tau = P_0 t_f \quad (11)$$

The rectangular pulse failure power P_0 is a function of duration t_f (the failure power-time model in the last section V.A.), so the failure criterion is written as:

$$\int_{\tau_0}^{\tau_0+t_f} P(\tau) d\tau = P_0(t_f) t_f \quad (12)$$

Note that the power-time integral must be performed in an assumed failure time span t_f ; otherwise, the integral of heat transfer function G cannot be eliminated. This is

intuitive; if the injected arbitrary wave's energy reaches $P_0(t_f) * t_f$ over a longer span than t_f , the junction temperature may still be lower than T_c because more heat has dissipated.

Equation (12) allows a devices' thermal failure to be evaluated without knowing its material, geometry, failure location or melting temperature. Only its tested failure model $P_0(t_f)$ and simulated time varying power profile $P(\tau)$ are needed. Equation (12) can be implemented with the following algorithm:

Assume a failure time t_f

Loop $\tau_0=0: \tau(end)-t_f$

$$E = \int_{\tau_0}^{\tau_0+t_f} P(\tau) d\tau$$

End loop

*Check if $\max(E) \geq P_0(t_f) * t_f$*

true: the device would fail

false: the device can survive;

update a new t_f value then start from the beginning

Equation (12) can be simplified further if $\tau_0 = 0$, or, if the highest power portion always occurs at the beginning of an injection (usually the case for an ESD event). The criterion, therefore, is simplified as:

$$\int_0^{t_f} P(\tau) d\tau = P_0(t_f) t_f \quad (13)$$

The interception point of the left and right sides of (13) stands for the failure time and destructive injection energy (but not the energy that heats the defect region).

Section VII contains examples of applying the failure criterion.

VI. SYSTEM-LEVEL SETUP, ESD GUN MODEL AND COMMON-MODE MODELING

A. System-Level Test Setup and Modeling

A contact-mode discharge on the DUT setup is shown in Fig. 15. A cellphone's battery charging cord, filtered with a ferrite, was connected to the cell phone's USB port as part of the return path. The cord's shielding at the other end was shorted to a large metal plane.

In such a test setup, the ESD current return path (common-mode path) and the ESD generator should be modeled in order to correctly calculate the ESD current within the circuitry under investigation.

B. System-Level Grounding Model

For the system test setup shown in Fig. 15, the connection between the cell phone's ground (metal frame) and the main ground plate can be modeled as shown in Fig. 16. The transmission lines TL1 and TL2 modeled the IO and Vcc nets on the double-sided flex circuit, respectively. The characteristic impedance was measured as 45Ω with a TDR. This impedance can also be calculated from the flex's 2D cross-sectional geometry. TL1 and TL2 were not referenced to the same metal; instead, their left sides were connected to the keyboard PCB's local ground, and their right sides were shorted to the main PCB's reference plane.

The transmission line TL3 modeled the flex's ground metal relative to the cellphone's body frame metal. The characteristic impedance of this common-mode path was measured as 120Ω .

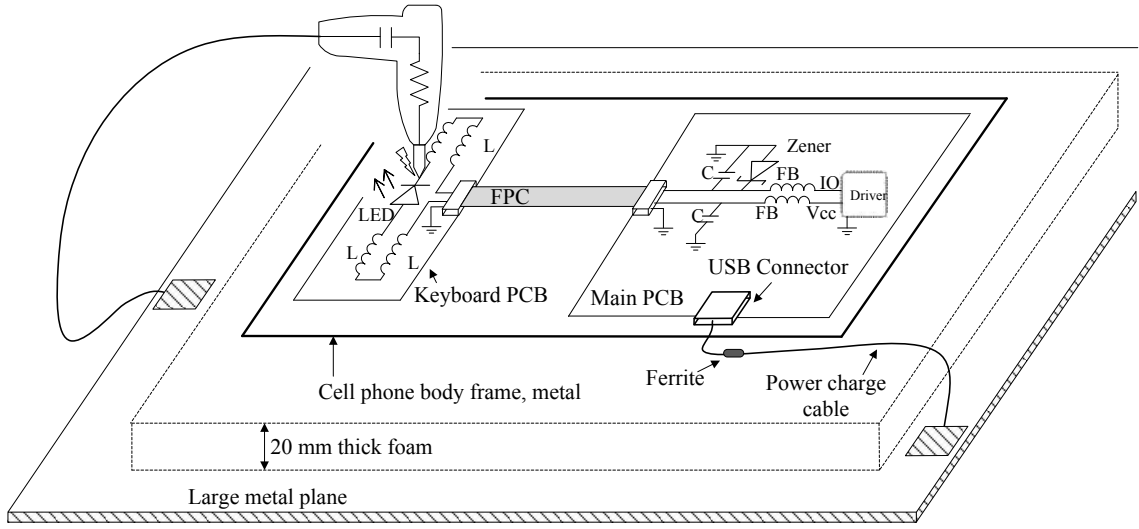


Fig. 15. The schematic of contact-mode discharge setup on the cellphone LED. The cellphone was grounded to a large metal plate via a USB charge cable. Inside the cellphone, the main and keyboard PCBs were well grounded to the body frame with metal screws and connector pins (hidden from sight). The keyboard PCB was grounded via flex connections.

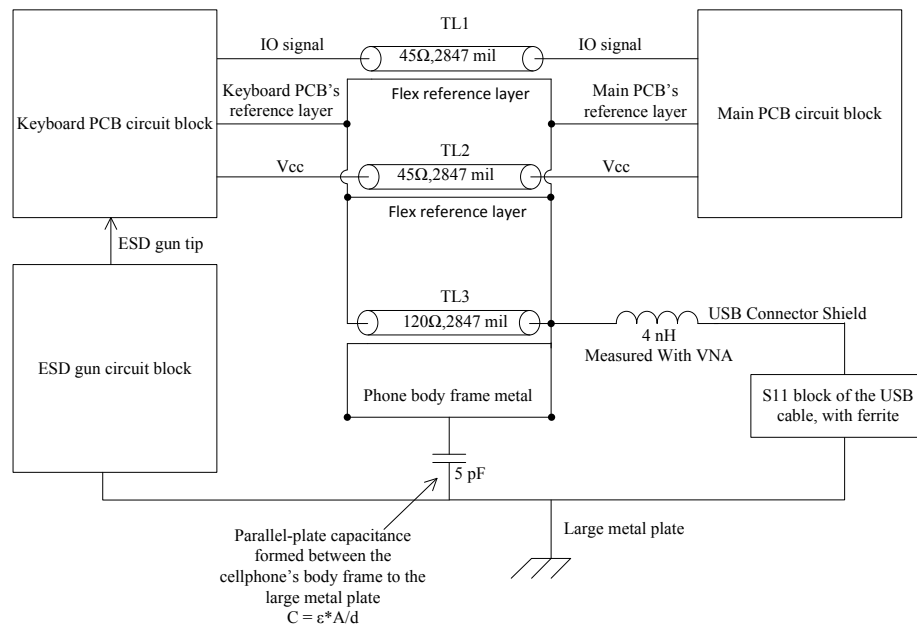


Fig. 16. System-level modeling structure

C. ESD Gun Model

An ESD generator, TESEQ NSG 438 [11], was used in this project. Its equivalent circuit model appears in Fig. 17, which was developed based on Wang's topology [13].

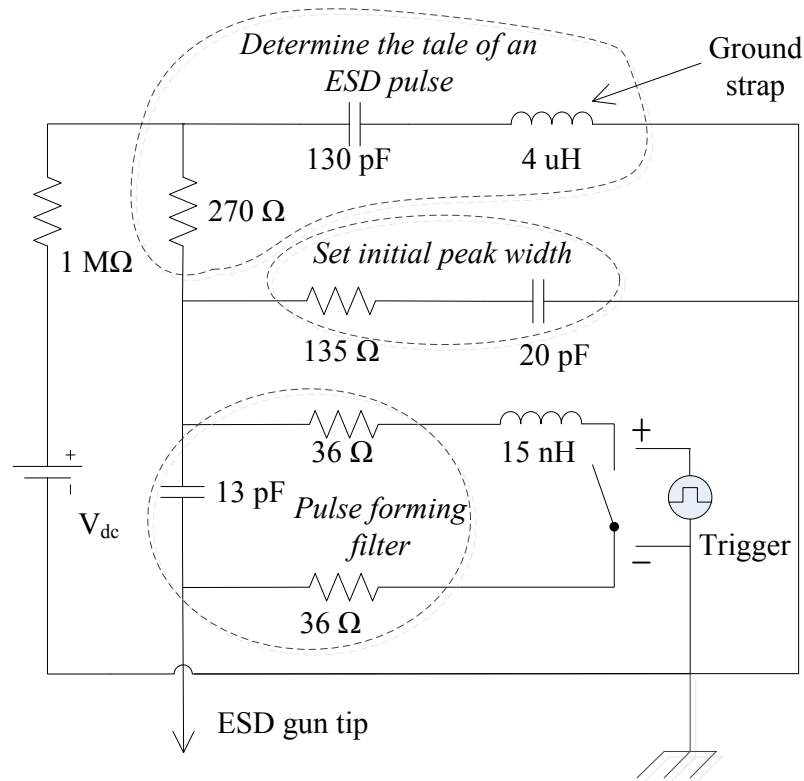


Fig. 17. Equivalent circuit model of the ESD generator

VII. SYSTEM-LEVEL SIMULATION RESULTS

A. System Model Validation

The system model was constructed by inserting all of the circuit models developed as described in Section IV, as well as the ESD gun model, into the system scheme shown in Fig. 17.

Fig. 18 shows one of our most challenging validation setups used for checking the

model's credibility and the robustness of the modeling methods. A Tektronix CT-6 probe was inserted in front of the IO pin to measure the ESD current flowing into the IC. To allow the current probe to be placed, an 8 mm long wire was soldered in-series to the IO pin. This wire introduced an additional $4nH$ inductance. The simulated current conformed to measurements reasonably well (Fig. 19).

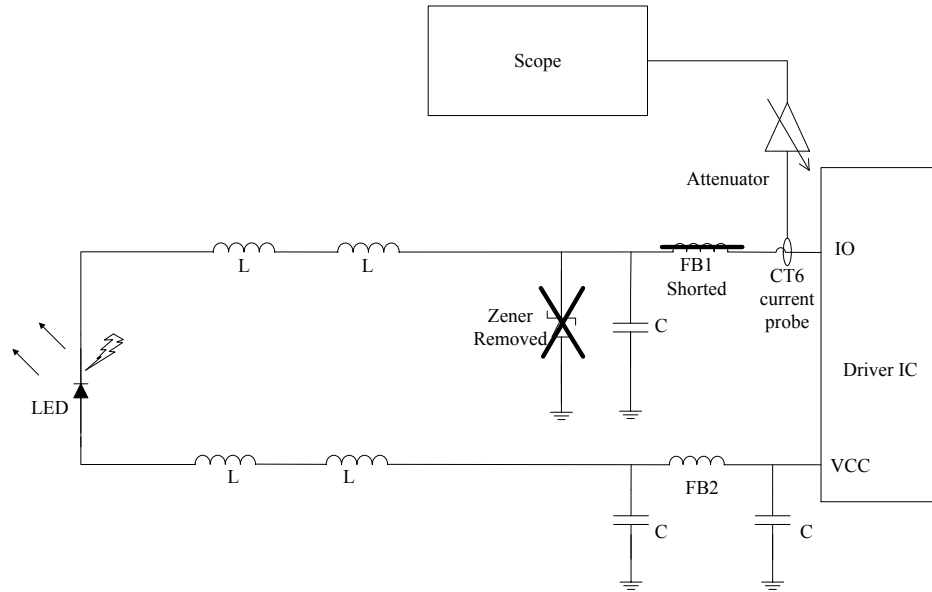


Fig. 18. Schematic of system-model validation setup. A CT-6 probe was inserted into the circuit to measure the IO pin's current under ESD injection. The protection diode and the ferrite bead ahead of the IO pin were removed and shorted, respectively, to determine the IO pin's ESD performance without external protections (this was also a challenging setup to validate the system model).

B. Application of the System Model for ESD Hard-Error Analysis

1) Transient Current Flows into the LED

One objective was to determine the conditions under which the LED would suffer damage. Calculating the destruction criteria (12) on the simulated power profile and the LED's failure model, respectively, showed that under +14kV, the LED would be damaged (Fig. 20), which agreed with our tested result. The checking algorithm also showed that under 15kV injection, the damage would occur within the first 5ns; under 14kV, the damage occurred at 32ns. Fig. 21 shows the result of the simplified checking algorithm (13).

2) Thermal Failure of the Driver IC

Another objective was to analyze the conditions under which the driver IC could survive without any external protection (same setup as shown in Fig. 18, but with a 10nF nonlinear capacitor in parallel to the LED to avoid LED destruction).

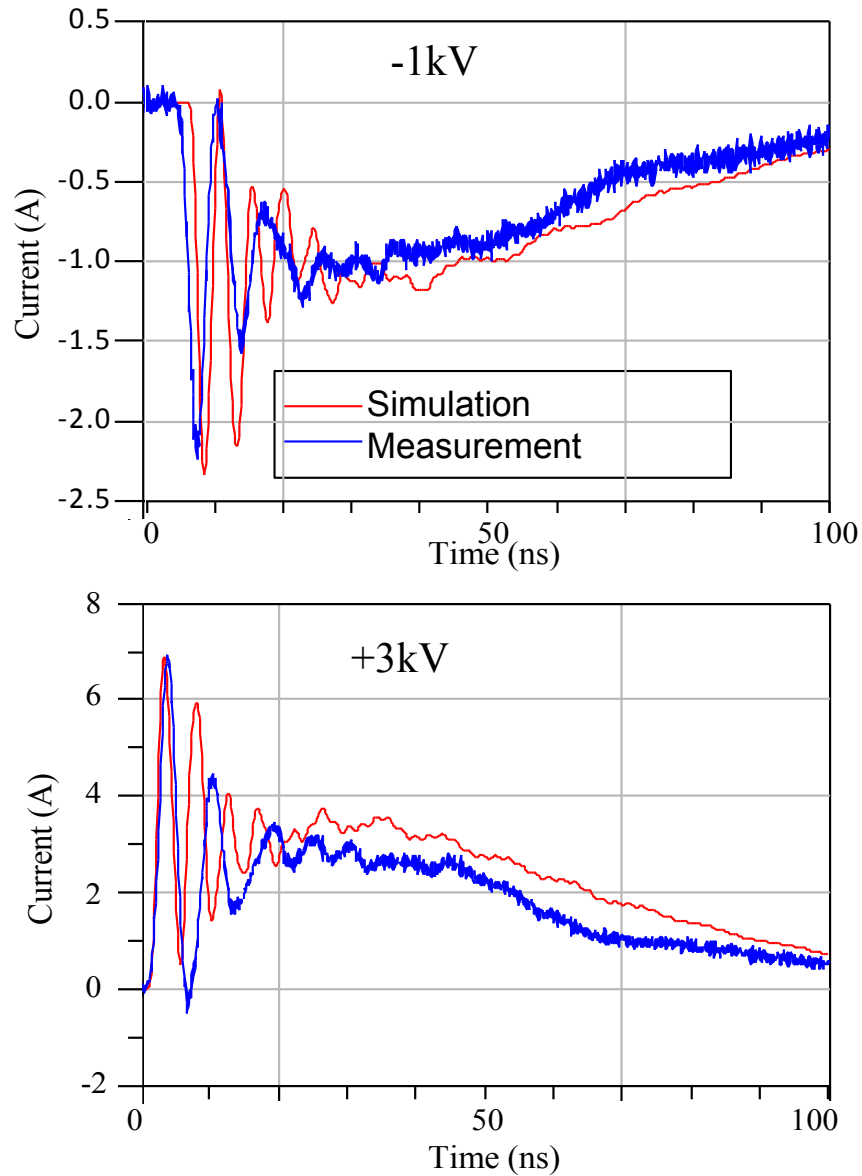


Fig. 19. IO pin's current under ESD injection at the cathode of the LED, simulated vs. measured.

By applying (12), we were able to predict that the driver IC could survive under 15kV but would not withstand a 16kV injection (Fig. 22). This prediction also agreed with our tested results.

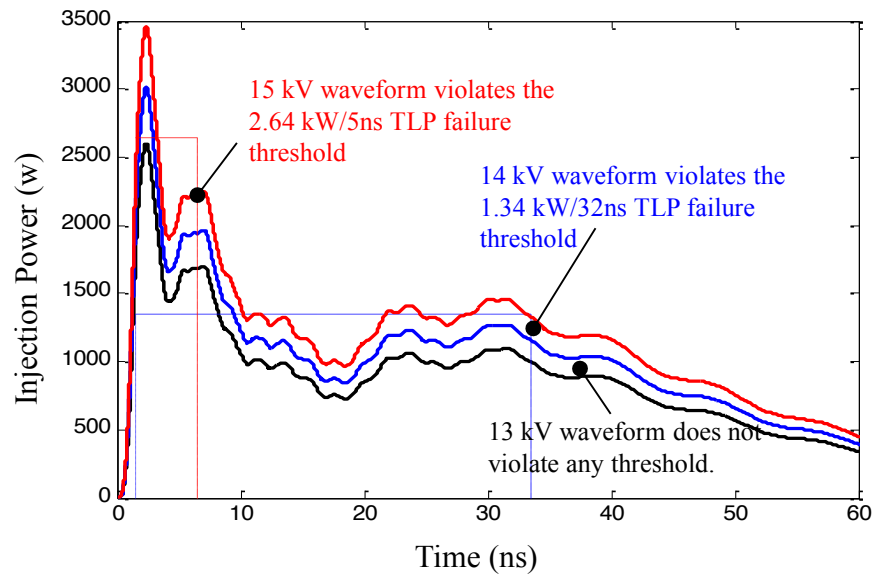


Fig. 20. Simulated injection power into LED under ESD contact-mode discharge at the LED's cathode. Using the damage criterion (12), it was shown that the LED could survive a 13kV injection but would begin to suffer damage upon the ESD exceeding 14kV. Our tested damage threshold was 14.5 ± 0.5 kV.

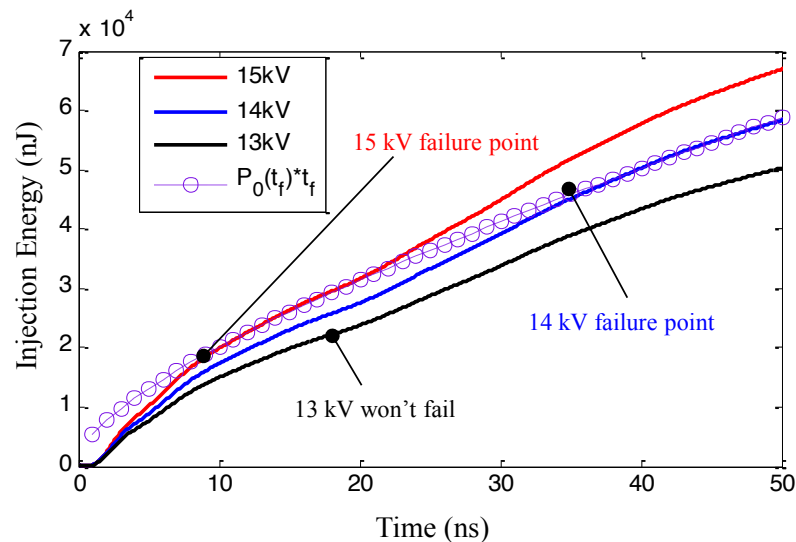


Fig. 21. Determine LED's damage with (13), which yielded the same conclusion with Fig. 20.

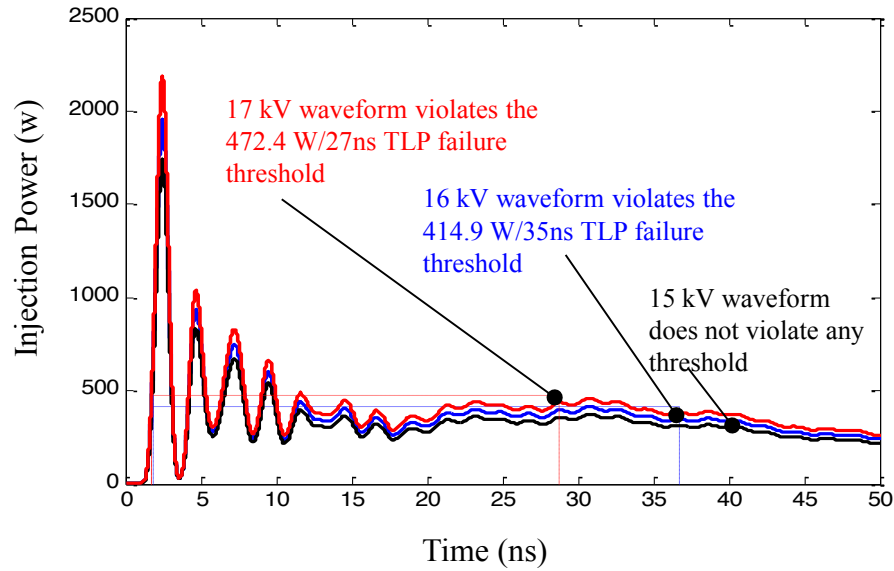


Fig. 22. Simulated injection power into LED driver's IO pin without any external protection under ESD contact-mode discharge at the LED's cathode (same setup as in Fig. 18). Simulation suggested that the LED can survive a 15kV injection but will begin to suffer damage when the ESD exceeds 16kV. Our tested damage threshold was

$$16.5 \pm 0.5 \text{ kV.}$$

VIII. CONCLUSION

The transient response of a real cell phone under IEC 61000-4-2 excitation was modeled. The proposed method features both high voltage/current and high speed (up to 3GHz) modeling of typical components, including R, L, C, ferrite, diodes and IC pins, as well as a complex return path model. The simulation result resembled the tested waveform at both the 1st and 2nd peaks of the IEC excitation.

The time-dependent destruction threshold of a semiconductor device can be obtained from the tested Wunsch-Bell model with rectangular waveforms. This model accounts for thermal-related junction failures, which have been proven to be the primary

cause of a semiconductor junction's failure mode under EOS.

To determine device failure under an arbitrary waveform based on knowledge of the TLP tested failure power/time relationship, one can identify whether or not any portion in the arbitrary waveform $P(\tau)$ injected the same amount of energy as a certain destructive rectangular pulse. Our proposed checking algorithm (12) and its simplified version (13) can be applied for IEC excitation scenarios. For other injection profiles in which the power peak does not occur at the very beginning of the whole waveform, (13) cannot be applied.

The proposed model is very suitable for both pre and post-design analysis due to its high computational efficiency. An engineer can quickly understand the holes in a design as long as off-the-shelf circuit models and failure threshold models can be provided readily by the device vendor. In addition to failure analysis, the system model also can be used to analyze ESD-induced interference in signal integrity problems, with an additional coupling path model.

REFERENCES

- [1] M. Scholz, S. Chen, G. Vandersteen, D. Linten, G. Hellings, M. Sawada, and G. Groeseneken, "Comparison of System-Level ESD Design Methodologies—Towards the Efficient and ESD Robust Design of Systems," *IEEE Trans. Device and Materials Reliability*, vol.13, no.1, pp.213-222, March 2013.
- [2] White Paper 3—System Level ESD, Part I, Industry Council on ESD, Target Levels, 2011.

- [3] H. Gossner, W. Simbürger, and M. Stecher, "System ESD robustness by co-design of on-chip and on-board protection measures." *Microelectronics Reliability*, vol.50, no.9, pp.1359-1366, 2010.
- [4] N. Monnereau, F. Caignet, D. Tremouilles, N. Nolhier, M. Bafleur, "A System-Level Electrostatic-Discharge-Protection Modeling Methodology for Time-Domain Analysis," *IEEE Trans Electromagnetic Compatibility*, vol.55, no.1, pp.45-57, Feb. 2013.
- [5] T. Li, J. Maeshima, H. Shumiya, D. J. Pommerenke, T. Yamada, K. Araki, "An application of utilizing the system-efficient-ESD-design (SEED) concept to analyze an LED protection circuit of a cell phone," in *Proc. IEEE EMC Symp.*, 2012, pp. 346-350.
- [6] IEC 61000-4-2 international standard, 1998.
- [7] T. Sekine, H. Asai, J.S. Lee, "Unified circuit modeling technique for the simulation of electrostatic discharge (ESD) injected by an ESD generator," in *Proc. IEEE EMC Symposium*, 2012, pp.340-345.
- [8] M. Scholz, S. Chen; S. Thijs, D. Linten, G. Hellings, G. Vandersteen, M. Sawada, and G. Groeseneken, "System-Level ESD Protection Design Using On-Wafer Characterization and Transient Simulations," *IEEE Trans. Device and Materials Reliability*, vol.14, no.1, pp.104-111, March 2014.
- [9] S. Bertonnaud, C. Duvvury, and A. Jahanzeb, "IEC system level ESD challenges and effective protection strategy for USB2 interfaces," in *Proc. EOS/ESD Symp.*, 2012, pp. 1–8.

- [10] L. Lou, C. Duvvury, A. Jahanzeb, and J. Park. "SPICE simulation methodology for system level ESD design." In EOS/ESD Symposium, 2010, pp.1-10.
- [11] TESEQ. [Online]. Available. <http://www.teseq.com/news/announcements/Teseq-Enhances-NSG-438-ESD-Simulator.php>
- [12] G. Notermans, S. Bychikhin, D. Pogany, D. Johnsson, and D. Maksimovic. "HMM-TLP correlation for system-efficient ESD design." *Microelectronics Reliability*, vol 52, no. 6, pp.1012-1019, 2012.
- [13] K. Wang; D. Pommerenke, R. Chundru, T. V. Doren, J. L. Drewniak, and A. Shashindranath, "Numerical modeling of electrostatic discharge generators," *IEEE Trans. Electromagnetic Compatibility*, vol.45, no.2, pp.258-271, May 2003.
- [14] A. Delmas, N. Nolhier, D. Trémouilles, M. Bafleur, N. Mauran, and A. Gendron. "Accurate transient behavior measurement of high-voltage ESD protections based on a very fast transmission-line pulse system." In *Proc. of 31st EOS/ESD Symposium*, 2009, pp. 165-172.
- [15] H. Li, V. Khilkevich, T. Li, D. Pommerenke, S. Kwon, and W. Hackenberger, "Nonlinear capacitors for ESD protection," *IEEE Electromagnetic Compatibility Magazine*, vol.1, no.4, pp.38-46, Fourth Quarter 2012.
- [16] S. Scheier and S. Frei. "Characterization and modeling of ESD-behavior of multi layer ceramic capacitors." *Electromagnetic Compatibility (EMC EUROPE)*, 2013 International Symposium on. IEEE, 2013.
- [17] S. Blonkowski, "Nonlinear capacitance variations in amorphous oxide metal-insulator-metal structures." *Applied Physics Letters*, vol.91, no. 17, 2007.

- [18] Advanced Design System (ADS). [Online]. Available.
<http://www.home.agilent.com/en/pc-1297113/advanced-design-system-ads>
- [19] Q. Yu, T.W. Holmes, and K. Naishadham, "RF equivalent circuit modeling of ferrite-core inductors and characterization of core materials," IEEE Trans. Electromagnetic Compatibility, vol.44, no.1, pp.258-262, Feb 2002.
- [20] D. Bowen, "Modeling and Testing of Ethernet Transformers," Ph.D. dissertation, ECE., UMD., College Park., MD, 2011.
- [21] D.C. Wunsch and R. R. Bell, "Determination of Threshold Failure Levels of Semiconductor Diodes and Transistors Due to Pulse Voltages," IEEE Trans. Nuclear Science, vol.15, no.6, pp.244-259, Dec. 1968.
- [22] D. M. Tasca, "Pulse power failure modes in semiconductors," IEEE Trans. Nuclear Science, vol.17, no.6, pp.364-372, 1970.
- [23] D. G. Pierce and D. L. Durgin. "An overview of electrical overstress effects on semiconductor devices," In Proceedings of the EOS/ESD Symposium, pp. 120. 1981.
- [24] H. S. Carslaw and J. C. Jaeger. Heat in solids. Vol. 19591. Clarendon Press, Oxford, 1959.
- [25] V. M. Dwyer, A. J. Franklin, and D. S. Campbell, "Thermal failure in semiconductor devices," Solid-State Electronics vol.33, no.5, pp.553-560, 1990.

SECTION 2. CONCLUSION

In the first paper, a realization averaging is demonstrated as a convenient method for phase resolved scan when multiple random sources exist. This technique is useful in real-world applications since a product usually includes multiple active circuits with different emission signatures. The noise sources can be separated by selecting a reference probe site deliberately during the scan. Important VNA settings for such a test have been discussed. The far field pattern caused by each source can be calculated accordingly from the scanned near field data. Moreover, the scanned data at semi-far field region also tells the emission source with the ESM algorithm.

In the second paper, a Huygens's source based methodology to model a complex noise structure by its electromagnetic equivalence has been validated. The term complex refers to that the noise source's mechanical structure, material properties and active behavior is so complex that they cannot be modeled directly. Application of this method is demonstrated on modeling an active LCD for calculating its RFI to the adjacent antenna, at 903.76MHz. The model can provide suggestive information for antenna and system grounding design optimization.

In the third paper, the transient response of a real cell phone under IEC 61000-4-2 excitation was modeled. The proposed method features both high voltage/current and high speed (up to 3GHz) modeling of typical components, including R, L, C, ferrite, diodes and IC pins, as well as a complex return path model. The simulation result resembled the tested waveform at both the 1st and 2nd peaks of the IEC excitation. The time-dependent destruction threshold of a semiconductor device can be obtained from the

tested Wunsch-Bell model with rectangular waveforms. This model accounts for thermal-related junction failures, which have been proven to be the primary cause of a semiconductor junction's failure mode under EOS. To determine device failure under an arbitrary waveform based on knowledge of the TLP tested failure power/time relationship, one can identify whether or not any portion in the arbitrary waveform $P(\tau)$ injected the same amount of energy as a certain destructive rectangular pulse.

VITA

Tianqi Li was born in Luonan, Shaanxi Province, P. R. China. He received the Bachelor of Science degree in Electronic-Communications Engineering (2004) from Tianjin University, Tianjin, P.R. China. He then worked as an electrical engineer with Huawei Technologies in Shenzhen, China till 2009. In 2012, he received the Master of Science degree in Electrical Engineering from Missouri University of Science and Technology. He took a half-year internship at Apple Computer, Cupertino, CA in 2013. In December 2014, he received his Ph.D. in Electrical Engineering from Missouri University of Science and Technology.

